

Mass Production of 2023 KMTNet Microlensing Planets I: Low Mass Ratio

YOON-HYUN RYU¹, ANDRZEJ UDALSKI², HONGJING YANG^{3,4}, KYU-HA HWANG¹,
WEICHENG ZANG⁵, YANG HUANG⁶, ANDREW GOULD⁷

AND

MICHAEL D. ALBROW⁸, PING CHEN^{9,10}, SUN-JU CHUNG¹, SUBO DONG^{11,12,13},
CHEONGHO HAN¹⁴, YOUN KIL JUNG^{1,15}, IN-GU SHIN³, YOSSI SHVARTZVALD¹⁶,
JENNIFER C. YEE⁵, SANG-MOK CHA^{1,17}, DONG-JIN KIM¹, SEUNG-LEE KIM¹,
CHUNG-UK LEE¹, DONG-JOO LEE¹, YONGSEOK LEE^{1,17}, BYEONG-GON PARK¹,
RICHARD W. POGGE^{7,18}

(THE KMTNET COLLABORATION)

PRZEMEK MRÓZ², RADOSŁAW POLESKI², JAN SKOWRON², MICHAŁ K. SZYMAŃSKI²,
IGOR SOSZYŃSKI², PAWEŁ PIETRUKOWICZ², SZYMON KOZŁOWSKI², KRZYSZTOF
ULACZYK¹⁹, KRZYSZTOF A. RYBICKI², PATRYK IWANEK², MARCIN WRONA^{2,20},
MARIUSZ GROMADZKI², MATEUSZ J. MRÓZ²

(THE OGLE COLLABORATION)

¹*Korea Astronomy and Space Science Institute, Daejeon 34055, Republic of Korea*

²*Astronomical Observatory, University of Warsaw, Al. Ujazdowskie 4, 00-478 Warszawa, Poland*

³*School of Science, Westlake University, Hangzhou, Zhejiang 310030, China*

⁴*Department of Astronomy, Tsinghua University, Beijing 100084, China*

⁵*Center for Astrophysics | Harvard & Smithsonian, 60 Garden St., Cambridge, MA 02138, USA*

⁶*School of Astronomy and Space Sciences, University of Chinese Academy of Sciences, 100049, Beijing, China*

⁷*Department of Astronomy, Ohio State University, 140 W. 18th Ave., Columbus, OH 43210, USA*

⁸*University of Canterbury, Department of Physical and Chemical Sciences, Private Bag 4800, Christchurch 8020, New Zealand*

⁹*Institute for Advanced Study in Physics, Zhejiang University, Hangzhou 310027, China*

¹⁰*Institute for Astronomy, School of Physics, Zhejiang University, Hangzhou 310027, China*

- ¹¹*Department of Astronomy, School of Physics, Peking University, 5 Yiheyuan Road, Haidian District, Beijing 100871, People’s Republic of China*
- ¹²*Kavli Institute of Astronomy and Astrophysics, Peking University, 5 Yiheyuan Road, Haidian District, Beijing 100871, People’s Republic of China*
- ¹³*National Astronomical Observatories, Chinese Academy of Science, 20A Datun Road, Chaoyang District, Beijing 100101, China*
- ¹⁴*Department of Physics, Chungbuk National University, Cheongju 28644, Republic of Korea*
- ¹⁵*National University of Science and Technology (UST), Daejeon 34113, Republic of Korea*
- ¹⁶*Department of Particle Physics and Astrophysics, Weizmann Institute of Science, Rehovot 7610001, Israel*
- ¹⁷*School of Space Research, Kyung Hee University, Yongin, Kyeonggi 17104, Republic of Korea*
- ¹⁸*Center for Cosmology and AstroParticle Physics, Ohio State University, 191 West Woodruff Ave., Columbus, OH 43210, USA*
- ¹⁹*Department of Physics, University of Warwick, Gibbet Hill Road, Coventry, CV4 7AL, UK*
- ²⁰*Villanova University, Department of Astrophysics and Planetary Sciences, 800 Lancaster Ave., Villanova, PA 19085, USA*

ABSTRACT

We initiate the systematic search for planets in the 2023 data of the Korea Microlensing Telescope Network (KMTNet), focusing on those planets found by the KMTNet AnomalyFinder with low preliminary estimates of the mass-ratio, $q < 2 \times 10^{-4}$. The 2023 season is the first for which the photometry of all events was re-reduced prior to the AnomalyFinder search, potentially increasing its sensitivity to planets. We find three strong low- q planet candidates, KMT-2023-BLG-0164 ($q \sim 1.3 \times 10^{-4}$), KMT-2023-BLG-1286 ($q \sim 1.9 \times 10^{-4}$), and KMT-2023-BLG-1746 ($q \sim 8 \times 10^{-5}$). KMT-2023-BLG-0164 is notable in that the source is projected on a very bright ($I = 16.0$) foreground star, which is either the planet’s host or (more likely) a companion to the host. We obtain a spectrum,

finding that its mass and distance are $M \sim 1.0 M_{\odot}$ and $D \sim 1.5$ kpc, the latter being the distance of the lens (D_L) regardless of whether the spectroscopic target is the host or its companion. We also analyze two other candidates, KMT-2023-BLG-0614 and KMT-2023-BLG-1593, which are unlikely to enter the statistical sample due to their ambiguous interpretations as possible non-planetary events.

Subject headings: gravitational lensing; micro

1. Introduction

1.1. From Mass-ratio Function to Planet Mass Function

The Korea Microlensing Telescope Network (KMTNet) is engaged in a decade-plus effort to assemble a statistical sample of bound planets discovered via microlensing observations toward the Galactic Bulge. The immediate objective is to measure the mass-ratio function, that is, the number of planets as a function of planet/host mass ratio, q . A longer-term objective is to measure the planet mass function.

The initial results for the mass-ratio function, based on 2016-2019 data, suggest that there are two populations of planets: one with mass ratios of order those of the Solar System’s gas giants (that is, Jupiter and Saturn), and the other with mass ratios of the Solar System’s solid-dominated planets (that is, Venus, Earth, Uranus, and Neptune) (Zang et al. 2025). This study was based on just 63 (out of the final 2016-2019 sample of 101) planets, so it is important to confirm (or contradict) its results using a larger sample.

At present, the longer-term objective of measuring the planet mass function is less well articulated compared to measuring the planet-host mass-ratio function, although Gould (2022) has initiated such an articulation. To turn a planet-host mass-ratio measurement (which are directly inferred from the microlensing light curves) into a planet-mass measurement, it is of course necessary to measure the host mass. In principle, this can be extracted from the light curve by measuring the Einstein radius θ_E and the microlens parallax, π_E , via $M = \theta_E / \kappa \pi_E$ where $\kappa = 4G/c^2 \text{au}$ (Gould 1992). In practice, while θ_E is measured in roughly 2/3 of all planetary events (Gould 2022), measurements of π_E are made only occasionally. Although measuring the mass function does not require knowledge of the mass of every planet within a statistical sample, determining a substantial majority of planet masses is essential.

1.2. Most Planet Masses Will Come From Late-time Imaging

Fortunately, there is a proven method that will eventually work for most microlensing planets, which was first applied to OGLE-2005-BLG-169 (Batista et al. 2015; Bennett et al. 2015): simply wait for the host star to be sufficiently separated from the source star that it had previously microlensed and take a high-resolution image. From the host-star flux (and an assumed mass-luminosity relation), one infers a relation between the mass of and the distance to the host. And from the host-source separation $\Delta\theta$ (and the length of time since the event Δt), one can infer their relative proper motion, $\mu_{\text{rel}} = \Delta\theta/\Delta t$, and hence the Einstein radius, $\theta_{\text{E}} = \mu_{\text{rel}}t_{\text{E}}$, where t_{E} is the Einstein timescale, which has already been derived from the light curve. Then, because the source distance D_S is approximately known, one obtains a second relation between the lens mass and distance, $\theta_{\text{E}}^2 = \kappa M[\text{au}(D_L^{-1} - D_S^{-1})]$. Combining the two relations yields separate determinations of M and D_L . See Figure 2 of Gould (2022).

There are numerous potential pitfalls to this approach, but Gould (2022) shows how these can be systematically resolved. The main difficulty today is that, even with the largest existing telescope (Keck), the FWHM in K -band is 55 mas. Thus, it has only been possible to separately resolve the two stars by waiting for an exceptionally long time, or by looking at systems for which the host and source have roughly equal brightness. As a result, by 2025, only 11 host mass measurements have been made using this method, the most recent being an event that occurred in 2014.¹ In particular, there are no such mass measurements for events from 2016 and later, that is, the period of the KMT project.

One possible solution would be to continue waiting, a strategy that we can assess by examining Figure 1, which shows all 24 mass measurements out of the 52 microlens planets that were observed during 2005-2014. These include 20 measurements using the two methods just described, that is, (1) Late-time high-resolution imaging (Batista et al. 2015; Bennett et al. 2015; Gould 2022) (“IMAGE”, red, 11); and (2) Combining light curve measurements of the microlens parallax (π_{E}) and Einstein radius (θ_{E}) to yield $M = \theta_{\text{E}}/\kappa\pi_{\text{E}}$ (Gould 1992) (“PAR”, green, 9); as well as a total of four measurements made using two other methods, (3) Combining light curve measurements of π_{E} with excess light, relative to the source flux derived from the light curve (Bennett et al. 2010), (“PAR+EXC-LIGHT”, cyan, 2); and (4)

¹These 11 are: OGLE-2005-BLG-169 (Batista et al. 2015; Bennett et al. 2015), OGLE-2012-BLG-0950 (Bhattacharya et al. 2019), OGLE-2005-BLG-071 (Bennett et al. 2020), MOA-2013-BLG-220 (Vandorou et al. 2020), MOA-2009-BLG-319 (Terry et al. 2021), MOA-2009-BLG-400 (Bhattacharya et al. 2021), OGLE-2013-BLG-0132 (Reksini et al. 2024), MOA-2008-BLG-379 (Bennett et al. 2024a), MOA-2007-BLG-192 (Terry et al. 2024), OGLE-2012-BLG-0563 (Bennett et al. 2024b), OGLE-2014-BLG-1760 (Reksini et al. 2025)

Mass derived from excess-light alone (Batista et al. 2014) (“EXC-LIGHT”, blue, 2).

1.3. EELT Will Dramatically Shorten Wait Times

From Figure 1, one sees that by waiting about 20 years after the KMTNet mass-ratio sample is collected, it will be possible to apply the imaging method to close to half the sample. And perhaps after another decade or two, the great majority of the sample will become accessible. However, long before this wait time expires (~ 2050 for the planets from the first full KMTNet observing season), a much larger telescope is expected to come on line: the 39m European Extremely Large Telescope (EELT), which completely changes the calculus.

Among the other three methods, the most promising would appear from Figure 1 to be “PAR”, i.e., $M = \theta_E / \kappa \pi_E$, with 9/52=17% mass measurements. However, due to the very different methods of identifying planet candidates in that earlier era (real-time by-eye recognition of promising events and – most often – real-time decision for intensive follow-up observations), the conditions for making such light-curve-based mass measurements were much more favorable than is the case for the current KMTNet sample. Thus, in the future, planet mass measurements will be dominated by the imaging method.

1.4. 2016-2019 Sample: Best for EELT First-light Mass-function Measurement

KMTNet has already assembled and fully analyzed a planet-host mass-ratio sample for 2016-2019, which contains 101 planets. This sample will be far more suitable for the first-light effort to systematically measure masses with EELT than planets from subsequent years, for example, the next four-year sample from 2021-2024. In 2030, hosts of planetary events from 2024 will have separated from the source star for 6 years, compared to 11 years for 2019 events. Because EELT is 3.9 times larger than Keck, its images will have a 3.9 times smaller FWHM than Keck, or 14 mas. Thus waiting for 6 years on EELT is equivalent to waiting 23 years on Keck. This is only slightly longer than the time span shown in Figure 1. Of course, the situation will be somewhat better for 2021-2023. But for the existing 2016-2019 sample, the EELT wait intervals will be equivalent to waiting 43 to 55 years on Keck. Hence, we may expect that the completeness of the mass measurements will be dramatically better than shown in Figure 1.

In this regard, there is a subtle effect that is not conveyed by Figure 1, These pre-2015 planets were overwhelmingly recognized “by eye”, whereas Jung et al. (2023) showed

(their Table 17) that $\sim 40\%$ of the KMT planet sample was found by the machine-based AnomalyFinder (Zang et al. 2021, 2022). And their Figure 20 shows that $\sim 65\%$ of non-caustic crossing planets (the main source of events without θ_E (and μ_{rel}) measurements) come from this 40% of the sample. These non- μ_{rel} planets pose a special challenge for the high-resolution follow-up program: if μ_{rel} is known, then one knows the exact annulus in which to search for the host, and a non-detection therefore directly yields an upper limit on the host flux that can be detected in this annulus. One can then decide whether this limit is adequate to the goal of measuring the mass function, or whether additional late-time imaging is warranted. However, if there is no μ_{rel} measurement from the microlensing event, a non-detection could be due to an abnormally low proper motion, potentially requiring additional observations. The only way to ameliorate this problem is to minimize the number of non-detections by having the first observation as late as possible. This again favors the 2016-2019 sample over later-year planets.

A third important advantage of the 2016-2019 events is that 10 of the hosts have mass measurements from *Spitzer* satellite-parallax observations, of which four (OGLE-2017-BLG-0406, OGLE-2017-BLG-1140, OGLE-2018-BLG-0596, and OGLE-2018-BLG-0932) have giant-star sources (Gould 2022). Due to the high (~ 100) to extremely high ($\sim 10^4$) source-host contrast ratios of these giant-source events, host-source separations of 5 or even more FWHM are required for host detection. Because *Spitzer* ceased operation after 2019, it does not provide supplementary information on the difficult class of giant-source events for any subsequent years. See Figure 6 from Gould (2022) for how microlens-parallax information can greatly improve a planet-mass measurement relative to imaging-only.

1.5. Can the 2016-2019 Sample Be Improved by Universal TLC Reductions?

In brief, there are compelling reasons to focus on the 2016-2019 sample when EELT first becomes available, and this raises the question of whether anything can be done to increase the size of this sample?

The answer is “plausibly yes”, but doing so would require long lead times and substantial effort, so that a cost-benefit analysis of this effort should be undertaken as soon as possible.

The KMT planets from 2016-2022 were found either by eye or with the AnomalyFinder by searching the event light curves from KMT’s standard pySIS (Albrow et al. 2009) reductions. These pipeline reductions are usually adequate to recognize the planetary anomaly, after which the data are subjected to tender loving care (TLC) re-reductions, and it is these that are presented in publications. However, it is likely that some planetary anoma-

lies are not recognizable from the pipeline reductions, in which case the data would not be re-reduced. With this in mind, Yang et al. (2024) developed an end-of-season pipeline by optimizing pySIS. This does not change the real-time photometry (and so does not impact the functioning of KMT alerts), but it does enable higher-quality end-of-season light curves and thereby potentially enables more end-of-season planets. In principle, one could extract the roughly 3000/year microlensing-event light curves from the KMT archives, apply the Yang et al. (2024) TLC pysis, rerun the AnomalyFinder on the result, and update the 2016-2019 sample. The human and machine effort would be considerable and would inevitably delay processing of subsequent seasons of planets (which would be 100% new discoveries).

The general goal of the “mass-production” and “complete-sample” papers, which contribute to assembling the underlying samples for such analyses, is to identify and analyze all events that have at least one “planetary” solution, defined as having a mass ratio $q \leq 0.03$. To this end, we would carry out an initial analysis of all candidates identified by AnomalyFinder and rereduce the data for all candidates that have at least one $q < 0.06$ solution. However, rereduction is unnecessary for 2023 data because (for the first time), the entire season’s light curves were rereduced prior to carrying out the search. For events with $0.03 < q < 0.05$, we would report the result, but not present a full analysis.

Here we begin the first assessment of the likely benefit of rereducing and reanalyzing the $\sim 12,000$ light curves from 2016-2019. The 2023 data have been re-reduced by the Yang et al. (2024) pipeline, and the AnomalyFinder has been run both on the old and new reductions. In the end, we must evaluate the whole sample of planets identified by both reductions, which requires the detailed analysis of more than 50 candidates. In this “mass production” paper, we begin this process by systematically investigating the 11 candidates with preliminary mass-ratio estimates of $\log q < -3.7$.

The 11 candidates² that we examined are KMT-2023-BLG-(0161,0164,0614,0705,0780,1286,1467,1593,1746,1790,1799). Of these 11, six were rejected because an examination of the images showed that the candidate planetary anomalies were not of astrophysical origin. These are KMT-2023-BLG-(0161,0705,0780,1467,1790,1799). This leaves five candidates, KMT-2023-BLG-(0164,0614,1286,1593,1746).

It is not our purpose to choose a final sample to measure the mass-ratio function or mass function, but rather to provide all the information necessary to do so. The main (though not the only) reason for excluding planetary candidates from such samples is that there are

²Excluding the five planetary events that have already been published, KMT-2023-BLG-(0416,1866,1896,2209) (Han et al. 2024a,b, 2025a,b) or are works in progress, KMT-2023-BLG-0382 (Krzysztof et al. in prep).

alternative non-planetary solutions, either binary-stellar solutions or binary-source (1L2S) solutions. As we will show, two of the five planetary candidates, KMT-2023-BLG-0614 and KMT-2023-BLG-1593, have such 1L2S solutions. In our view, these two are unlikely to be included in subsequent, statistical analyses, but we nevertheless present complete analyses of these events.

In Section 2, we present our general methodology. In Section 3, we present the analysis of five planetary candidates, three of which are secure planetary events, while the remaining two are ambiguous. We present statistical estimates of the physical parameters of the three secure planetary systems in Section 4, and in Section 5, we briefly summarize our results.

2. Methodology

2.1. Observations

All of the planetary candidates in this paper were identified in AnomalyFinder searches of KMT events that were announced by the KMT AlertFinder (Kim et al. 2018) as the 2023 season progressed. KMTNet observes from three 1.6m telescopes (Kim et al. 2016) that are equipped with ($2^\circ \times 2^\circ$) cameras at CTIO in Chile (KMTC), SAAO in South Africa (KMST), and SSO in Australia (KMTA), mainly in the *I* band, with 60 second exposures, but with 9% of the observations in the *V* band. The data were initially reduced using pySIS (Albrow et al. 2009), a form of difference image analysis (DIA, Tomaney & Crotts 1996; Alard & Lupton 1998). As described in Section 1, all light curves were reduced using the TLC pySIS pipeline of Yang et al. (2024) prior to applying AnomalyFinder, and we manually examined the images during the anomaly to rule out image artifacts as a potential explanation for the light-curve deviations.

Two of the five events reported here were also alerted by other surveys: KMT-2023-BLG-1286 (OGLE-2023-BLG-0803) was alerted by OGLE, and KMT-2023-BLG-0164 (OGLE-2023-BLG-0116, MOA-2023-BLG-107) was alerted by both OGLE and MOA. We include the OGLE data in the analysis of both of these events. However, we do not include the MOA data because the scatter is too large to help constrain either the anomaly itself or the parallax measurement of KMT-2023-BLG-0164.

The OGLE data were obtained using a 1.4 deg^2 camera on the 1.3m Warsaw telescope at Las Campanas Observatory in Chile and were primarily 100 second exposures in standard Cousins *I*-band, with a small minority of *V*-band observations.

The photometric error bars were renormalized according to the prescription of Section

2.1 of Yee et al. (2012) on an observatory-by-observatory basis. Briefly, the original errors, σ_i , are expressed (or re-expressed) in magnitudes, and the renormalization is expressed in terms of two parameters (k, e_{\min}) as $\sigma' = k\sqrt{\sigma^2 + e_{\min}^2}$. First an initial model is found. Then, $k = 1$ is held constant while e_{\min} is adjusted until the cumulative distribution of χ^2 (sorted by magnification A_i) is approximately a straight line, and the total $\chi_{\text{tot}}^2(e_{\min})$ is noted for this choice of e_{\min} . Finally, k is set for each data by $k = \sqrt{N_{\text{data}}/\chi_{\text{tot}}^2(e_{\min})}$, where N_{data} is the number of data points for that observatory, so that χ^2 per degree of freedom is approximately unity for each observatory separately and for all observatories together.

As far as we are aware, there were no follow-up observations, either by follow-up groups or the surveys themselves.

Table 1 gives the event names, observational cadences Γ , discovery dates and sky locations. Because each of the five events was first discovered by KMT, we use the KMT name for all five, following the standard naming convention.

2.2. Light-curve Modeling

Our approach to analyzing events is identical to that described in several earlier mass-production papers that report collections of AnomalyFinder planets and planet candidates. Here we repeat, essentially verbatim, the “preamble” to the light-curve analysis of one these papers, Ryu et al. (2023), in order to permit the reader direct access to the relevant formulae and descriptions.

All of the events in this paper can be analyzed to a first approximation as 1L1S events, which are characterized by three Paczyński (1986) parameters, (t_0, u_0, t_E) , that is, the time of lens-source closest approach, the impact parameter (normalized to the Einstein radius, θ_E), and the Einstein-radius crossing time

$$t_E = \frac{\theta_E}{\mu_{\text{rel}}}; \quad \theta_E = \sqrt{\kappa M \pi_{\text{rel}}}, \quad \kappa \equiv \frac{4G}{c^2 \text{ au}} \simeq 8.14 \frac{\text{mas}}{M_{\odot}}. \quad (1)$$

Here, M is the mass of the lens, $(\pi_{\text{rel}}, \boldsymbol{\mu}_{\text{rel}})$ are the lens-source relative parallax and proper motion, $\mu_{\text{rel}} \equiv |\boldsymbol{\mu}_{\text{rel}}|$, and $nLmS$ means “ n lenses and m sources”.

A 2L1S model always requires at least three additional parameters (s, q, α), that is, the separation (normalized to θ_E) and mass ratio of the two lens components, as well as the angle between the line connecting these and the direction of $\boldsymbol{\mu}_{\text{rel}}$. If there are finite-source effects due to the source approaching or crossing caustic structures that are generated by the lens, then one must also specify $\rho \equiv \theta_*/\theta_E$, where θ_* is the angular radius of the source.

For 1L2S models, which can generate featureless bumps that can be mistaken for 2L1S “planets” (Gaudi 1998), the minimal number of parameters is 6, including $(t_{0,1}, t_{0,2})$ and $(u_{0,1}, u_{0,2})$ for the two times of closest approach and impact parameters, respectively, t_E for the Einstein timescale, and q_F , that is, the flux ratio of the two sources in the I -band. In many cases, one or both of the two normalized source radii must be specified, $\rho_1 = \theta_{*,1}/\theta_E$ and $\rho_2 = \theta_{*,2}/\theta_E$. More complex models involving orbital motion of the binary-source system may also be needed.

If the microlens parallax effect can be detected (or constrained), then one should include the microlens parallax vector (Gould 1992, 2000, 2004),

$$\boldsymbol{\pi}_E = \frac{\pi_{\text{rel}}}{\theta_E} \frac{\boldsymbol{\mu}_{\text{rel}}}{\mu_{\text{rel}}}, \quad (2)$$

which is normally expressed in equatorial coordinates $\boldsymbol{\pi}_E = (\pi_{E,N}, \pi_{E,E})$. In these cases, one usually must also fit, at least initially, for the first derivatives in time of the lens angular position, $\boldsymbol{\gamma} = [(ds/dt)/s, d\alpha/dt]$, because $\boldsymbol{\pi}_E$ and $\boldsymbol{\gamma}$ can be correlated or even degenerate. In these cases, we restrict such fits to $\beta < 0.8$, where (An et al. 2002; Dong et al. 2009),

$$\beta \equiv \frac{\kappa M_{\odot} \text{yr}^2}{8\pi^2} \frac{\pi_E}{\theta_E} \gamma^2 \left(\frac{s}{\pi_E + \pi_s/\theta_E} \right)^3, \quad (3)$$

and where π_s is the source parallax.

In our initial heuristic analyses, we often predict s_{\pm}^{\dagger} and α from the morphology of the light curve (Hwang et al. 2022; Ryu et al. 2022),

$$s_{\pm}^{\dagger} = \frac{\sqrt{4 + u_{\text{anom}}^2} \pm u_{\text{anom}}}{2}; \quad \tan \alpha = \frac{u_0}{\tau_{\text{anom}}}, \quad (4)$$

under the assumption that the anomaly occurs when the source crosses the binary axis. Here, $u_{\text{anom}} = \sqrt{\tau_{\text{anom}}^2 + u_0^2}$, $\tau_{\text{anom}} = (t_{\text{anom}} - t_0)/t_E$, t_{anom} is the midpoint of the anomaly, and the “ \pm ” refers to major/minor image perturbations. If there are two solutions, with normalized separation values s_{\pm} , as often occurs (see Zhang et al. 2021 for a theoretical discussion of such degeneracies), we expect that the empirical quantity $s^{\dagger} = \sqrt{s_+ s_-}$ (without subscript) will be approximately equal to the subscripted quantity from Equation (4).

We also note that Hwang et al. (2022) showed that for minor-image perturbations, the mass ratio can be estimated by

$$q = \left(\frac{\Delta t_{\text{dip}}}{4 t_E} \right)^2 \frac{s \sin^2 \alpha}{u_{\text{anom}}} = \left(\frac{\Delta t_{\text{dip}}}{4 t_E} \right)^2 \frac{s}{|u_0|} |\sin^3 \alpha|, \quad (5)$$

where Δt_{dip} is the full width of the depression in the light curve relative to the 1L1S model.

Finally we sometimes report the “source self crossing time”, $t_* \equiv \rho t_E$. We note that this is a derived quantity and is not fit independently.

2.3. Source Properties

Our evaluation of the source properties exactly follows the goals and procedures of previous “mass production” papers. In this introduction, we therefore repeat, essentially verbatim, the corresponding introduction from Section 4.1 of Ryu et al. (2023). In particular (as in Section 2.2), we seek to document all procedures and notation without referring the reader to other papers.

We analyze the color-magnitude diagram (CMD) of each event, primarily to measure θ_* and so to determine

$$\theta_E = \frac{\theta_*}{\rho}; \quad \mu_{\text{rel}} = \frac{\theta_E}{t_E}. \quad (6)$$

We follow the method of Yoo et al. (2004). We first find the offset of the source from the red clump

$$\Delta[(V - I), I] = [(V - I), I]_S - [(V - I), I]_{\text{cl}}. \quad (7)$$

We adopt $(V - I)_{\text{cl},0} = 1.06$ from Bensby et al. (2013) and evaluate $I_{\text{cl},0}$ from Table 1 of Nataf et al. (2013), based on the Galactic longitude of the event, which yields the dereddened color and magnitude of the source,

$$[(V - I), I]_{S,0} = [(V - I), I]_{\text{cl},0} + \Delta[(V - I), I]. \quad (8)$$

Next, we transform from V/I to V/K using the VIK color-color relations of Bessell & Brett (1988), and we apply the color/surface-brightness relations of Kervella et al. (2004a,b) to obtain θ_* . After propagating the measurement errors, we add 5% to the error in quadrature to take account of systematic errors due to the method as a whole.

To obtain $[(V - I), I]_S$, we always begin with pyDIA reductions (Albrow 2017), which put the light curve and field-star photometry on the same system. With two exceptions (see below), we determine $(V - I)_S$ by regression of the V -band data on the I -band data, and we determine I_S by regression of the I -band data on the best-fit model. For three of the five events analyzed in this paper, there is calibrated OGLE-III field-star photometry (Szymański et al. 2011). For these three cases, we transform $[(V - I), I]_S$ to the OGLE-III system. For the two remaining cases, we work in the instrumental KMT pyDIA system.

For KMT-2023-BLG-0614 and KMT-2023-BLG-1593, the sources are too faint in the V band to measure the source color from the light curve. We therefore employ a different technique, as described in Sections 3.4.3 and 3.5.3.

The CMDs are shown in Figure 2.

The elements of these calculations are summarized in Table 2. In all cases, the source flux is that of the best solution. Under the assumption of fixed source color, θ_* scales as

$10^{-\Delta I_S/5}$ for the other solutions, where ΔI_S is the difference in source magnitudes, as given in the Tables of Section 3. The inferred values (or limits upon) θ_E , and μ_{rel} are given in the individual events subsections below, where we also discuss other issues, when relevant.

2.4. Bayesian Analysis

None of the three planets and two candidate planets have sufficient information to precisely specify the host mass and distance. For any given solution, we can incorporate Galactic-model priors into standard Bayesian techniques to obtain estimates of the host mass M_{host} and distance D_L , as well as the planet mass M_{planet} and planet-host projected separation a_{\perp} . See Jung et al. (2021) for a description of the Galactic model and Bayesian techniques. However, in most cases we still have to decide how to combine these separate estimates into a single “quotable result”.

We show the posterior distributions for the host mass and distance in the individual subsections below, and

we tabulate the posterior estimates and uncertainties for M_{host} , M_{planet} , D_L , and a_{\perp} in Section 4.

3. Analysis of Selected Events from the KMTNet 2023 Season

3.1. KMT-2023-BLG-0164

Figure 3 shows an otherwise standard 1L1S light curve with Paczyński (1986) parameters $(t_0, u_0, t_E) = (51.23, 0.072, 75 \text{ day})$, superposed by a $\Delta t_{\text{dip}} = 3.0$ day dip, centered at $t_{\text{anom}} = 63.0$.

3.1.1. Heuristic Analysis

These parameters imply $\tau_{\text{anom}} = 0.157$, $u_{\text{anom}} = 0.173$, and thus

$$\alpha = 204.6^\circ; \quad s_{\perp}^{\dagger} = 0.917; \quad q = 9 \times 10^{-5}. \quad (9)$$

3.1.2. Static Analysis

The grid search on the (s, q) plane returns two solutions, whose refinements with all parameters set free are shown in Table 3. We see that $\alpha = (204.8^\circ, 204.7^\circ)$ in the two solutions, while $s^\dagger \equiv \sqrt{s_+ s_-} = 0.913$, which are both extremely close to the heuristic predictions. The two values of q are also in qualitative agreement with Equation (9). Because the anomaly takes the form of shallow dip, we expect only upper limits on the normalized source flux ρ . Qualitatively, we expect $\rho t_E \lesssim (\Delta t_{\text{dip}}/2) |\sin \alpha|$, or $\rho \lesssim 8 \times 10^{-3}$. As seen from Table 3, this expectation proves qualitatively correct, but we defer quantitative discussion of the limit on ρ until Section 3.1.3.

Within the context of static models, the degeneracy between the inner and outer solutions is often broken when the source trajectory is close to planet-host axis, as for example, $|\sin \alpha| \simeq 0.4$ in the present case. This is because the source trajectory is substantially closer (or farther) from the vertically symmetric caustic at the beginning of the anomaly than at the end, so that the anomaly is not time-symmetric about its center. See the caustic-geometry panels in Figure 3. Such would appear to be true for KMT-2023-BLG-0164 for which the inner model is favored by $\Delta\chi^2 = 50$. However, because the event is relatively long, $t_E \sim 75$ day, both parallax and orbital motion can play a significant role, and these additional parameters may absorb some or all of the distinguishing features of the two light-curve models. Therefore, we investigate both the inner and outer solutions in the parallax analysis, to which we now turn.

3.1.3. Parallax Analysis

As is almost always the case (except for some extremely long events), for each standard solution, there are two parallax solutions, which differ by the sign of u_0 . See Smith et al. (2003) for an explanation and Figure 4 of Gould (2004) for the sign convention. Hence, there are a total of four solutions, which are summarized in Table 4 and illustrated in Figure 3. As described in Section 2.2, we simultaneously fit for the first derivatives of the planet position due to its orbital motion $\boldsymbol{\gamma} = [(ds/dt)/s, d\alpha/dt]$. Table 4 shows that in each of the four solutions, $\boldsymbol{\pi}_E$ is very well localized, and this is further illustrated by Figure 4. In both $u_0 > 0$ solutions, $\boldsymbol{\pi}_{E,+} = (\pi_{E,N}, \pi_{E,E}) \simeq (0.52, 0.16)$, while in both $u_0 < 0$ solutions, $\boldsymbol{\pi}_{E,-} \simeq (0.71, 0.15)$. That is, the magnitude and direction (north through east), ψ_π , are $(\pi_E, \psi_\pi)_+ = (0.54, 18^\circ)$ and $(\pi_E, \psi_\pi)_- = (0.73, 12^\circ)$, respectively. These angles are close to the Galactic plane which is inclined by 30° relative to Equatorial north.

The large value of π_E implies that the lens almost certainly lies in foreground disk unless

it is an extreme substellar object. That is, $\pi_{\text{rel}} = \pi_{\text{E}}^2 \kappa M = 0.3 \text{ mas} (\pi_{\text{E}}/0.6)^2 (M/0.1 M_{\odot})$. In fact, we will show in Section 3.1.5 that the source is blended with a bright foreground star that is almost certainly either the lens itself or a stellar companion to it. The Gaia proper motion for this object (and so, in either case, the proper motion of the lens) is $\boldsymbol{\mu}_l = (\mu_{l,N}, \mu_{l,E}) = (+0.2, -1.9) \text{ mas yr}^{-1}$. Thus, if the source has a typical bulge proper motion, that is, similar to SGR A*, $\boldsymbol{\mu}_{\text{sgrA}^*} = (-5.6, -2.7) \text{ mas yr}^{-1}$, then the lens-source proper motion would be $\boldsymbol{\mu}_{\text{rel}} \sim (5.8, 0.8) \text{ mas yr}^{-1}$, implying $\mu_{\text{rel}} \sim 5.9 \text{ mas yr}^{-1}$ and $\psi \sim 8^\circ$. Thus, the resulting direction is very similar to the two values of $\psi_{\pi, \pm}$ derived above.

With these broad expectations in mind, we now turn to the constraints on ρ . Figure 5 shows a scatter plot of $\Delta\chi^2$ versus ρ from the Monte Carlo fit. As also indicated in Table 4, for the outer solutions $\rho < 2.3 \times 10^{-4}$ at the 3σ level. Such low values would be in tension with the previous arguments because

$$\rho \equiv \frac{\theta_*}{\theta_{\text{E}}} = \frac{\theta_*}{\mu_{\text{rel}} t_{\text{E}}} = 7.4 \times 10^{-4} \left(\frac{\mu_{\text{rel}}}{6 \text{ mas yr}^{-1}} \right)^{-1}, \quad (10)$$

where we have incorporated the measurement, $\theta_* = 0.92 \mu\text{as}$, from Table 2.

That is, given the characteristic expected proper motion derived above, ρ would be 3.2 times larger than its 3σ limit.

This tension could be resolved by one of several paths. First, the source could be moving at 13 mas yr^{-1} relative to SGR A* (approximately in the direction of negative Galactic rotation), which is extremely unlikely ($p \sim 10^{-5}$). Second, the χ^2 deviation could be greater than 3σ , but according to Figure 5, it would have to be much greater. Third, one of the two inner solutions could be correct.

The last alternative seems obviously correct because comparison of Equation (10) and Table 4 shows that they are compatible at the 3σ level. Moreover, they are only mildly in tension at 2σ (or even 1σ), which could easily be accommodated by normal motion of the source within the bulge.

Thus, the most likely interpretation is that one of the two inner solutions is correct, and that $\mu_{\text{rel}} \sim 6 \text{ mas yr}^{-1}$, which would imply

$$M = 0.25 M_{\odot} \left(\frac{\mu_{\text{rel}}}{6 \text{ mas yr}^{-1}} \right) \left(\frac{\pi_{\text{E}}}{0.6} \right)^{-1}; \quad \pi_{\text{rel}} = 0.74 \text{ mas} \left(\frac{\mu_{\text{rel}}}{6 \text{ mas yr}^{-1}} \right) \left(\frac{\pi_{\text{E}}}{0.6} \right). \quad (11)$$

That is, at the fiducial values of Equation (11), the lens would be a middle M dwarf at $D_L \sim 1.2 \text{ kpc}$.

Unfortunately, such a lens would be far too faint ($I \sim 20$) to account for the blended light ($I \sim 16$), which we have identified as being either the lens itself or its companion.

One obvious solution is that blended light is the companion to the lens. This would still be in some tension with the Gaia measurement because the lens parallax would still be $\pi_l = 0.8$ mas, whereas Gaia reports $\pi_{\text{Gaia}} = 0.28 \pm 0.17$ mas. However, Gaia also reports a large “RUWE” value, 2.25, which parameterizes the excess scatter of the data about the 5-parameter astrometric solution. Such large RUWE values imply substantially less reliability for results reported by Gaia (even though Gaia renormalizes its error bars by the RUWE), as studied by Jung et al. (2022). Note, in particular, their discussion of the four events listed in their Table 14 that have large RUWE values, $1.75 \leq \text{RUWE} \leq 2.15$. At RUWE=2.25, the excess astrometric scatter of KMT-2023-BLG-0164 is bigger than any of the four documented problem cases.

In fact the large RUWE may tend to support the conjecture that the bright Gaia star is a companion to the lens rather than the lens itself. The main cause of high RUWE is the presence of an unresolved star near or somewhat beyond the Gaia point-spread function (PSF) of the target star, which is asymmetric and approximately (135×375) mas at I band. When the short axis of the mirror is aligned with the position angle of the interloper, its light maximally contributes to the mean astrometric position of the measurement, whereas when the long axis of the mirror is so aligned, the interloper contributes much less. Thus, a binary companion at, for example, a separation of 150 mas, would induce excess RUWE scatter through this mechanism. This would represent a projected separation of 180 AU in the current example.

This is a plausible scenario, but it is also possible that the proper motion is substantially faster than assumed in Equation (11), for example, $\mu_{\text{rel}} = 12 \text{ mas yr}^{-1}$. While this would require a mildly improbable source proper motion ($p \sim 5\%$), the resulting mass, $M \sim 0.5 M_{\odot}$, and distance, $D_L \sim 0.6 \text{ kpc}$, would yield a lens apparent magnitude of $I \sim 16$, which is approximately what is observed. Of course, the larger lens parallax $\pi_l \sim 1.6$ mas would be in even greater conflict with the Gaia measurement, but again, we cannot place too much trust in such a high-RUWE measurement.

3.1.4. Robustness Tests

We note that the inferences just derived rest critically on two broad physical pieces of information. First, the parallax is relatively large, $\pi_E \sim 0.6$, and second, the lens proper motion μ_l is small compared to the difference between the mean motion of disk and bulge stars, that is $\mu_l \ll |\boldsymbol{\mu}_{\text{sgrA*}}| \sim 6 \text{ mas yr}^{-1}$, which implies, roughly speaking, $\mu_{\text{rel}} \sim \mu_{\text{sgrA*}}$.

We now examine whether these two pieces of information are really robust. Regarding π_E , the main questions are: could the putative π_E be of non-astrophysical origin (that is, the result of systematic errors in the measurement), or could it be due to astrophysical effects

that are unrelated to the lens distance?

To address the first of these, we examine separately data from the four observatories, $n = 1, 2, 3, 4 \rightarrow$ (KMTC, KMTS, KMTA, OGLE). We start by excluding the part of the light curve that is significantly affected by the anomaly ($60 < \text{HJD}' < 70$) and fitting the remaining light curve to a five parameter 1L1S model ($t_0, u_0, t_E, \pi_{EN}, \pi_{EE}$), thus deriving the best fit $(a_1, a_2)^n = \boldsymbol{\pi}_E$ and the parallax covariance matrix, c_{ij}^n , for each of the four observatories³. Here $\text{HJD}' = \text{HJD} - 2460000$. For each of the six resulting (n, m) pairs we calculate $\chi_{nm}^2 = \sum_{ij} (a^n - a^m)_i (a^n - a^m)_j (c^n + c^m)_{ij}^{-1}$. We find that the three pairs of (KMTS, KMTA, OGLE) are all perfectly consistent ($\chi^2 \lesssim 1$), whereas the other three pairs (each containing KMTC) each show indications of tension. We therefore consider two complementary data sets, namely KMTC-only and Complement(KMTC) = (KMTS+KMTA+OGLE). And, for completeness, we also consider each of the other three data sets and its complement. To form the complement, we calculate $b^{\text{comp},n} = \sum_{m \neq n} b^m$, $d^{\text{comp},n} = \sum_{m \neq n} d^m$, $b^m = (c^m)^{-1}$, $d_i^m = \sum_j b_{ij}^m a_j^m$, $c^{\text{comp},n} = (b^{\text{comp},n})^{-1}$, $a_i^{\text{comp},n} = \sum_j c_{ij}^{\text{comp},n} d_j^{\text{comp},n}$. The results are shown in Table 5. The main point is that while the two solutions (KMTC and Complement(KMTC)) have different best-fit values of $\boldsymbol{\pi}_E$, these values are not qualitatively different. Hence, even if one were to conclude that, for example, KMTC should be excluded as “corrupted” by systematic errors, the arguments given above would not be qualitatively affected. Moreover, we find that the same test of difference in data sets given above yields $\chi_{\text{KMTC,Complement}}^2 = 5.7$. This would appear to have a (two-dimensional) false-alarm probability of $p = \exp(-\chi^2/2) = 6\%$, which would itself be marginal evidence for a systematic disagreement. But we must also consider that we have effectively considered four “trials”, that is, four configurations of the data (excluding each of the four observatories). Hence, the significance of this “conflict” is $< 1\sigma$. Therefore, in our further analysis we do not exclude any of the data.

The only known type of astrophysical “contamination” of the $\boldsymbol{\pi}_E$ measurement would be “xallarap”, that is, distortions of the light curve due to orbital motion of the source about an unseen companion (Griest & Hu 1992; Han & Gould 1997). In principle, xallarap can perfectly mimic any real parallax effect provided that the 7 Kepler parameters of the binary-source orbit match those of Earth, including, in particular that the orientation and phase of the orbit mimic the parallax ellipse induced by Earth’s motion about the Sun. However, the more precisely that xallarap can be measured, and the tighter the resulting “agreement”, the less probable is the xallarap interpretation (Poindexter et al. 2005). As usual, we do not

³Of course, a proper measurement of $\boldsymbol{\pi}_E$ requires inclusion of the planetary parameters, and hence of the anomalous data. However, here we are searching for evidence of systematic errors via discrepancies between independent data sets, not $\boldsymbol{\pi}_E$ itself. And this comparison can only be made for the 1L1S light curve because the OGLE data do not have sufficient coverage, by themselves, to derive the planetary parameters.

fit for all seven Kepler parameters, but assume a circular orbit.

Figure 6 shows χ^2 as a function of assumed xallarap period P , after marginalizing over all possible orbit-orientation parameters, (α, δ) . As expected if the actual cause of the light-curve distortions is parallax (that is, Earth’s motion about the Sun), the best-fit xallarap period should be $P = 1$ yr. Relative to the best parallax fit (Table 4), there is an improvement of $\Delta\chi^2 \sim 6$. Under the assumption of Gaussian statistics (which is optimistic for microlensing), this can occur with probability $p = \exp(-\Delta\chi^2/2) = 5\%$ for two degrees of freedom (dof), which reflects only mild tension.

Nevertheless, we conduct a further test: we allow the xallarap orientation, (α, δ) , to vary freely, while holding the xallarap period fixed at $P = 1$ yr. In an ideal world, the best fit would be at the ecliptic coordinates of the event $(\alpha, \delta) = (\lambda, \beta) \rightarrow (269.8^\circ, -8.3^\circ)$. We find a best fit of $(\alpha, \delta) = (262^\circ, -5^\circ)$, which is good agreement. As a matter of due diligence, we repeat the 1-year xallarap fit with the eccentricity and time of periastron fixed at the terrestrial values, but (as one might expect), this does not materially affect the result.

Finally, we examine whether the apparently low Gaia $\mu_l = 1.9 \pm 0.2 \text{ mas yr}^{-1}$ could be an artifact of whatever measurement problems caused the high excess-scatter parameter, $\text{RUWE} = 2.25$. Recall that we regarded the Gaia parallax measurement, $\pi_l = 0.28 \pm 0.17 \text{ mas}$, as not providing a strong constraint due to this same high RUWE. And, of course, the Gaia parallax and proper-motion derive from the same 5-parameter fit.

However, there are three reasons that the same argument does not apply to μ_l . First, we expect that while the excess scatter can reflect systematic errors that are larger than the reported statistical errors (even after renormalization by the RUWE factor that is already included in the Gaia result), these errors are still most likely caused by a semi-random process. That is, they are due to excess light entering the aperture in semi-random amounts due to semi-random orientations of the telescope. Therefore, it is plausible to represent these errors as a further inflation of the reported statistical errors, say, to be conservative, by a factor five. However, whereas the effective errors of the parallax measurement would then be $\pi_l = 0.28 \pm 0.85 \text{ mas}$ (thus, for example, allowing any $D_l \gtrsim 1 \text{ kpc}$), the same inflation would lead to $\mu_l = 1.9 \pm 1.0 \text{ mas yr}^{-1}$, which would not qualitatively change the argument given in Section 3.1.3 at all.

The second reason that the same argument does not apply is that the parallax is a scalar while the proper motion is a vector. That is, as an exercise, let us assume that the true proper motion is much larger but has been corrupted by a random systematic error of arbitrary size (even though it is difficult to imagine the physical process that would then yield the low observed scatter of the fit). This systematic error would be in a random direction

relative to the true proper motion of the object. However, there is only a relatively small range of angles for which this would lead to a substantial reduction of the reported μ_l relative to the “true” (that is, putative) one.

The third reason is that we have an independent check on the Gaia proper motion from OGLE. Specifically, in Gaia DR3 (Gaia Collaboration et al. 2023), the blend (or technically, the blend augmented by $\sim 4\%$ of its light from the source) is listed as having

$$\pi_b = 0.277 \pm 0.169, \quad \boldsymbol{\mu}_b = (\mu_{b,E}, \mu_{b,N}) = (-1.91, +0.18) \pm (0.19, 0.13) \text{ mas yr}^{-1}, \quad (12)$$

with a correlation coefficient of 0.356, and a RUWE=2.25 parameter. We have already discussed the implications of the high RUWE parameter above and, and we do not repeat that discussion here. On the other hand, based on its own internal measurement, OGLE reports the blend proper motion (but not the parallax) as

$$\boldsymbol{\mu}_b = (\mu_{b,E}, \mu_{b,N}) = (-2.05, -0.20) \pm (0.07, 0.05) \text{ mas yr}^{-1}, \quad (OGLE). \quad (13)$$

Unlike Gaia, OGLE is ground-based rather than space-based, but it does have two major advantages relative to Gaia: a far larger number of data points and two-dimensional imaging, which is far less susceptible to contamination by bright neighboring stars. As a result, the formal errors are roughly three times smaller and the poorly understood systematics signaled by the large Gaia RUWE number are less of a concern. While the 0.4 mas yr^{-1} difference between Equations (12) and (13) is formally significant (albeit marginally), it is very small compared to the characteristic, $\sim 3 \text{ mas yr}^{-1}$, dispersion of bulge sources, which dominates the dispersions in the lens-source relative proper motion.

Thus, the possibility that μ_l is substantially larger than the value reported by Gaia, is effectively ruled out.

3.1.5. CMD Analysis

The main issue that requires special care for this event is the blended light. As can be seen in Figure 2, the blend is 3.5 mag brighter than the source and lies on the “foreground” main sequence. That is, it suffers substantially less extinction and reddening due to a smaller dust column, compared to the majority of stars in the CMD, which lie in the bulge. These characteristics imply that the blend dominates the “catalog star” that was monitored in order to find the microlensing event, but is unrelated to the “source star” whose light was impacted by the event. In particular, the blend is not a companion to the source, so it must be either the lens itself, a companion to the lens, or an ambient field star that happens to be projected close to the event. The measured offset between the event and the baseline object (which is overwhelmingly dominated by the blend) is $\Delta\theta = 70 \text{ mas}$ as measured by KMT

and $\Delta\theta = 44$ mas as measured by OGLE. Given that the surface density of foreground stars brighter than the blend is $n = 3.0 \text{ arcmin}^{-2}$, the probability of such a chance projection, even using the larger of these two values is $p = n\pi\Delta\theta^2 = 1.3 \times 10^{-5}$. Thus, the blend is almost certainly either the lens itself or a companion to the lens.

In preparation for Section 3.1.6, we note that the proper motion in Equation (12) can be expressed in Galactic coordinates as

$$\boldsymbol{\mu}_b = (\mu_{b,l}, \mu_{b,b}) = (-0.89, +1.75) \pm (0.17, 0.16) \text{ mas yr}^{-1}, \quad (14)$$

with a correlation coefficient of -0.48 . In that section we will make use of the full inverse covariance matrix

$$b_{\mu,\text{gaia}} = \begin{pmatrix} 43.37 & 23.02 \\ 23.02 & 53.77 \end{pmatrix} (\text{mas yr}^{-1})^{-2}. \quad (15)$$

3.1.6. Bayesian Analysis

The Bayesian analysis of KMT-2023-BLG-0164 is subject to four separate constraints, which differ for each of the four solutions shown in Table 4. Two of constraints come directly from that table: on t_E and $\boldsymbol{\pi}_E$. For both of these parameters, the central values are those listed in the table, but for $\boldsymbol{\pi}_E$, we express the error ellipse as an inverse covariance matrix, b , and evaluate $\chi^2 = \sum_{ij} a_i b_{ij} a_j$ where a_i is the difference between the measured parallax and the random realization of the Galactic model.

The third constraint is the limit on ρ , which we characterize as an envelope function based on Figure 5. That is, for each event realization, we evaluate θ_E based on the mass of the host and the distances to the source and lens. We then evaluate $\rho = \theta_*/\theta_E$ using the central value of θ_* given in Table 2, and finally we evaluate χ^2 based on the envelope function derived from Figure 5. We then repeat this for 17 values of θ_* , weighting each according to the error bar, $\sigma(\theta_*)$, given in Table 2, that is, $\theta_{*,k} = \theta_{*,\text{best}} + (k/2)\sigma(\theta_*)$, ($k = -8, \dots, +8$).

The fourth constraint is on the lens proper motion. As discussed in Sections 3.1.4 and 3.1.5, the Gaia star is almost certainly either the lens itself or a companion to it, and in either case its proper motion is the same as that of the lens. However, due to the high RUWE value, the Gaia measurement error is almost certainly underestimated. To take account of this, we adopt Equation (14) for the central value of the lens proper motion (in Galactic coordinates), but we degrade the error ellipse of this determination relative to Equation (15) by setting $b_{\mu,l} = b_{\mu,\text{gaia}}/10$. We note that the OGLE measurement that was reported in Equation (13), which is much more precise, is then consistent with this inflated error at the 1σ level.

Finally, each random realization (including the 17 separate realizations of θ_*) is weighted by $\exp(-\chi^2/2)$, where $\chi^2 = \chi_{t_E}^2 + \chi_{\pi_E}^2 + \chi_{\rho}^2 + \chi_{\mu,l}^2$.

The posterior distributions of the lens mass and distance are shown in Figure 7. As we tabulate in Section 4, the two “outer” models are strongly inconsistent with the Galactic-model priors, that is, they have $p = 0.000$ weight in the penultimate column. The physical reasons for this were anticipated in detail in Section 3.1.3. Both of the remaining (that is, the “inner”) solutions have M-dwarf hosts that lie a few kpc from the Sun. See Figure 7 and Section 4.

Finally, we predict the two-dimensional (color-magnitude) posterior of the lens light, assuming a main-sequence lens and accounting for the increasing dust column as a function of distance. This is shown for the two inner solutions in Figure 8. The color and magnitude of the blend (which did not enter the Bayesian analysis in any way) are shown as an “X”. Note that while, in both cases, the “most likely” lenses are much fainter and redder than the blend, the blend is consistent with the overall distribution at the 1–2 sigma level.

3.1.7. *Spectrum of KMT-2023-BLG-0164*

Based on the analysis of Section 3.1.3, as confirmed by Section 3.1.6, we recognized that the nature of KMT-2023-BLG-0164 could be significantly clarified by a high-resolution spectrum, which was feasible with a relatively large telescope due to the brightness of the blend, $(V, I)_b = (17.55, 16.00)$, as derived from OGLE-III calibrated photometry.

On UT 2025-07-18, P.C. obtained spectroscopic data consisting of two 450 s exposures with a spectral resolution $R \sim 1000$ using the Inamori Magellan Areal Camera and Spectrograph (IMACS; Dressler et al. 2011) mounted on the 6.5-m Magellan-Baade telescope under excellent conditions ($\sim 0.5''$ seeing). The spectrum (Figure 9) directly resolves one major issue, the lens distance, and it also opens the path to a more complete understanding of the planetary system.

The light from the target is dominated by a star with $(T_{\text{eff}}/\text{K}, \log g, [\text{Fe}/\text{H}]) = (5703 \pm 153, 4.46 \pm 0.17, 0.10 \pm 0.15)$, which is similar to the Sun $(5770, 4.44, 0)$. We infer a blend mass, absolute magnitude and color of $(M_{\text{bl}}/M_{\odot}, M_I, (V - I)_0) = (0.98 \pm 0.07, 4.17 \pm 0.33, 0.78 \pm 0.05)$.

The stellar atmospheric parameters are estimated by template matching using a χ^2 minimization technique, with templates drawn from the MILES spectral library (Sánchez-Blázquez et al. 2006). We restrict the fits to the spectral range from 4600 to 6800 Å. The

blue part of the spectrum is excluded due to its low signal-to-noise ratio, while the red part is excluded because of the limited wavelength coverage of MILES and the scarcity of absorption features in that region. In addition, the Na I D doublet region and the diffuse interstellar band (DIB) features at $\lambda\lambda 5780$ and 6283 \AA are masked in the fitting, as they are affected by interstellar absorption. All MILES templates are convolved to a resolution of $R \sim 1000$ to match the resolution of the observed spectra. The final atmospheric parameters are computed as the average values from the five best-fitting templates with the lowest χ^2 values. The associated uncertainties are taken as the standard deviations among these five solutions.

Using the derived stellar atmospheric parameters, we estimated the stellar mass, intrinsic color $(V - I)_0$, and I -band absolute magnitude of the target by adopting a Bayesian method similar to that of Huang et al. (2022). For the theoretical models, we employed the PARSEC isochrones (Bressan et al. 2012; Marigo et al. 2017). This approach yields the posterior probability distribution function (PDF) for each parameter. The final adopted value of each parameter is taken as the median of the corresponding posterior PDF, and the associated uncertainty is defined as half of the difference between the 84th and 16th percentiles.

Assuming for the moment that all the light from the observed blend is due to this spectroscopic star (we have already subtracted the small amount of source light), then its observed $(V - I)_b = 1.55$ requires $E(V - I) = 1.55 - 0.78 = 0.77$ of reddening from dust along the line of sight. From Table 2, the ratio of total-to-selective extinction toward the source is $(A_I/E(V - I))_s = (1.68/1.44) = 1.17$. In principle, the dust behind the target could have different properties than the nearby dust. However, because the event is at relatively high latitude, $b = -4.0$, most of the dust column is relatively near the Sun, implying that this effect is likely to be small. In any case we ignore it and conclude that the extinction is $A_{I,b} = 0.77 \times 1.17 = 0.90$, which implies a distance of $D_L = 10^{(I - M_I - A_I)/5 - 2} = 1.53 \text{ kpc}$ and therefore a lens-source relative parallax of

$$\pi_{\text{rel}} = \frac{\text{au}}{D_L} - \frac{\text{au}}{D_S} \simeq 0.53 \text{ mas.} \quad (16)$$

Notice that this estimate of π_{rel} does not depend on the spectroscopic target actually being the host of the planet, it only depends on this object being at the same distance as the host, that is, either the host itself or a stellar companion of the host. We already argued in Section 3.1 against the only other two logical possibilities, that is, a companion to the source or a random field star projected along the line of sight. We note that if, for example, the target were not the host and the actual host accounted for 20% of the blend light, then the I -band flux would be 20% less bright than we have inferred and so D_L would be 10% bigger. However, even this possibility would have only a modest impact on π_{rel} .

There are various errors associated with this estimate, but for the moment we ignore

these and just ask whether this spectroscopic object is broadly consistent with being the lens, given the other information that is available.

Regardless of whether the spectroscopic target is the lens or its companion, Equation (16) implies that

$$\pi_E = \sqrt{\frac{\pi_{\text{rel}}}{\kappa M}} = 0.26 \left(\frac{M}{0.98 M_\odot} \right)^{-1/2}; \quad \theta_E = \sqrt{\kappa M \pi_{\text{rel}}} = 2.1 \text{ mas} \left(\frac{M}{0.98 M_\odot} \right)^{1/2}. \quad (17)$$

The strongest constraint comes from the microlens parallax measurement (Figure 4). We have already argued in Section 3.1.3 that the two “outer” solutions are ruled out, which was confirmed from the formal Bayesian analysis by their $p = 0.000$ posterior probabilities. The “inner(+)” solution has a smaller parallax, but as can be seen from Figure 4, it is still in 4.5σ conflict with a value of $\pi_E = 0.26$. From the parallax formula, there are only two ways to “increase” π_E : either increase π_{rel} or decrease M . There is hardly any room for the latter, given the inferred temperature. Increasing π_{rel} (decreasing D_L) would require increasing M_I or A_I or decreasing I . Small changes in any of these are possible, but just to move from 4.5σ to 3σ would require a combined change of 0.9 mag in these three quantities. Thus, if reconciliation is possible, it would be primarily by “blaming” the light-curve measurement of π_E , not the interpretation of the spectrum. Such problems in microlensing parallaxes (and microlensing light curves more generally) are hardly unknown, but before settling on this explanation, we explore other evidence and other possibilities.

Next, we examine the problem of the implied source proper motion, $\boldsymbol{\mu}_s$. We have

$$\boldsymbol{\mu}_{\text{rel,geo}} = \frac{\theta_E}{t_E} = \frac{2.1 \text{ mas} (M/0.98 M_\odot)^{1/2}}{70 \text{ d}} = 11.0 \text{ mas yr}^{-1} \left(\frac{M}{0.98 M_\odot} \right)^{1/2}, \quad (18)$$

where we have inserted the scaled value of θ_E that was just derived. Note that we have made explicit that this is the geocentric proper motion because our information about the source and lens proper motions is, by contrast, in the heliocentric frame. The two are related by,

$$\Delta \boldsymbol{\mu}_{\text{rel}} = \boldsymbol{\mu}_{\text{rel,hel}} - \boldsymbol{\mu}_{\text{rel,geo}} = \frac{\pi_{\text{rel}}}{\text{au}} \mathbf{v}_{\perp,\oplus}; \quad \mathbf{v}_{\perp,\oplus}(N, E) = (+3.88, +12.71) \text{ km s}^{-1}, \quad (19)$$

where $\mathbf{v}_{\perp,\oplus}$ is the projected velocity of Earth at t_0 . Inserting the above value of $\pi_{\text{rel}} = 0.53 \text{ mas}$ yields $\Delta \boldsymbol{\mu}_{\text{rel}}(N, E) = (0.43, 1.42) \text{ mas yr}^{-1}$.

We now seek to express $\boldsymbol{\mu}_s$ in the bulge frame (in which the underlying distribution is approximately symmetric about (0,0)). We write $(\boldsymbol{\mu}_l - \boldsymbol{\mu}_s)_{\text{hel}} = \boldsymbol{\mu}_{\text{rel,geo}} + \Delta \boldsymbol{\mu}_{\text{rel}}$, implying $(\boldsymbol{\mu}_{s,\text{hel}} - \boldsymbol{\mu}_{\text{SgrA}^*}) = -\boldsymbol{\mu}_{\text{rel,geo}} - \Delta \boldsymbol{\mu}_{\text{rel}} - \boldsymbol{\mu}_{\text{SgrA}^*} + \boldsymbol{\mu}_{l,\text{hel}}$, OR

$$(\boldsymbol{\mu}_{s,\text{hel}} - \boldsymbol{\mu}_{\text{SgrA}^*}) = \left[-11.0 \left(\frac{M}{0.98 M_\odot} \right)^{1/2} \hat{\mathbf{n}} + (+4.54, +2.98)_{l,b} \right] \text{ mas yr}^{-1}, \quad (20)$$

where $\hat{\mathbf{n}}$ is the direction of the parallax vector $\boldsymbol{\pi}_E$. From the inner(+) solution as represented in Table 4, the best fit for this direction is 17° (north through east), which is 13° north of the Galactic plane. Inserting this value into Equation (20), and adopting its fiducial mass, yields $(\boldsymbol{\mu}_{s,\text{hel}} - \boldsymbol{\mu}_{\text{SgrA*}}) = (-6.18, +0.51) \text{ mas yr}^{-1}$. As the one-dimensional dispersion of bulge stars is slightly less than $\sigma = 3 \text{ mas yr}^{-1}$, such a value would be in slightly more than 2σ tension with the expectation for bulge sources, which is (other things being equal) acceptable.

Finally, we note that, given the value $\theta_* = 0.92 \mu\text{as}$ from Table 2, the inferred value of $\rho = \theta_*/\theta_E$ as a function of lens mass is $\rho = 4.4 \times 10^{-4} (M/0.98 M_\odot)^{-1/2}$. From Table 4 (see Figure 5 for more detail), this is acceptable for the fiducial mass, although it degrades slowly toward lower masses.

Thus, to briefly summarize, the value of $\boldsymbol{\pi}_E$ inferred under the assumption that the spectroscopic target is the host is in 4.5σ tension with the light-curve analysis, which could only be resolved by suggesting that there was a major problem with the light-curve data. This is possible, but we have already shown in Section 3.1.4 that the various individual data sets are basically consistent. By contrast, the inferred values of $\boldsymbol{\mu}_s$ and ρ are only in mild tension.

On the other hand, we should note that for Bayesian range tabulated in Section 4 for the inner(+) solution, $M/M_\odot = 0.44 \pm 0.22$, the inferred $\boldsymbol{\pi}_E$ is perfectly consistent, as are the inferred $\boldsymbol{\mu}_s$ and ρ . Moreover, even though no direct information about D_L was injected into the Bayesian analysis, the posterior range $D_L = 1.16_{-0.33}^{+0.64} \text{ kpc}$, is in excellent agreement with the spectroscopic determination of the lens distance.

We conclude that the balance of evidence favors that the spectroscopic target is a binary companion to the host, rather than the host itself.

3.1.8. Host Mass From Future Adaptive Optics (AO) Observation

It will be possible measure the host mass of KMT-2023-BLG-0164 and to distinguish whether it is the spectroscopic target or its companion using AO on extremely large telescopes (ELTs), most plausibly the EELT. The method is slightly different from the one pioneered by Batista et al. (2015) and successfully applied to a dozen other cases, as summarized in Section 1 and analyzed in depth by Gould (2022). The method is closer in spirit to the one first advocated by Paczyński (1995), in which he pointed out that the lens mass could be derived from (in modern notation) the measurements of π_{rel} and μ_{rel} . That is,

$$M = \frac{(\mu_{\text{rel}} t_E)^2}{\kappa \pi_{\text{rel}}}. \quad (21)$$

For Paczyński, both μ_{rel} and π_{rel} would be obtained astrometrically, but in our case, π_{rel} is obtained spectroscopically, not necessarily from the lens itself but most likely from a more luminous stellar companion.

It is far from clear that late-time AO observations will even detect the lens. For example, it would likely be several mag fainter than the spectroscopic target and therefore, if the binary orbit is too tight (for example, ~ 20 au or ~ 13 mas), it would remain hidden in the glare of the spectroscopic target, indefinitely. Nevertheless, because μ_{rel} for this companion is essentially the same as for the host, it can be derived from two late-time AO observations that separately resolve the spectroscopic target and the source. The spectroscopic target is $\Delta I = 3.5$ mag brighter than the source, and has a similar spectral type, so similar colors. Therefore, the contrast ratio is $\Delta K = \Delta I - \Delta E(I - K) \simeq \Delta I - (6/7)\Delta A_I \simeq 2.85$, where we have adopted $\Delta A_I \sim 0.77$ and assumed $A_I \sim 7 A_K$, which is generally valid over the KMT fields.

Given EELT’s diffraction-limited K -band FWHM of 14 mas, this contrast ratio should be observable at EELT first light, perhaps 2030, when the source and lens will be separated by about $\Delta\theta = [77(M/0.98 M_{\odot})^{1/2} + 8]$ mas. If, as seems likely, the host cannot be directly observed, the proper motion can still be derived from the difference in positional offsets between two epochs that are separated by one or two years.

3.2. KMT-2023-BLG-1286

Figure 10 shows an otherwise standard 1L1S light curve with Paczyński (1986) parameters $(t_0, u_0, t_E) = (118.79, 0.13, 14.7 \text{ day})$, punctuated by a $\Delta t_{\text{bump}} = 0.1$ day bump, centered at $t_{\text{anom}} = 118.48$.

3.2.1. Heuristic Analysis

These parameters imply $\tau_{\text{anom}} = -0.021$, $u_{\text{anom}} = 0.13$, and thus

$$\alpha = 99.2^\circ; \quad s_+^\dagger = 1.067, \quad (22)$$

3.2.2. Light-curve Analysis

The grid search on the (s, q) plane returns two competitive solutions, plus a third (“resonant”) solution that is disfavored by $\Delta\chi^2 > 100$, but which we include for completeness. The refinements of these three solutions, with all parameters set free, are shown in Table 6. We see that $\alpha = 99.1^\circ$ in both competitive solutions, while $s^\dagger \equiv \sqrt{s_+ s_-} = 1.070$, which are both extremely close to the heuristic predictions.

Although the bump is smooth, it is sharply peaked, which indicates that the source passes close to a cusp but probably not over it. This is true of all three models, as seen in the insets to Figure 10. This narrow peak allows ρ to be measured, despite the lack of a caustic crossing. See Table 6. For comparison, OGLE-2016-BLG-1195 provides a classic example of this geometry (Bond et al. 2017; Shvartzvald et al. 2017). Nevertheless, because the errors in this measurement are non-Gaussian (in particular, asymmetric), we display their functional form in Figure 11.

In the resonant model, the peak is produced by an approach to an off-axis cusp. However, as seen in Figure 10, this off-axis cusp approach does not reproduce the small “dips” that flank the bump and are clearly seen in the data. This is the origin of the $\Delta\chi^2 > 100$ that rules out this model.

Because the anomaly is a non-caustic-crossing bump, we also check for 1L2S models. Although the best such model reproduces the main features of the bump, it fails to reproduce the dips that flank the bump. This failure is very similar to that of the resonant model in both morphology (see Figure 10) and in $\Delta\chi^2$ (see Table 6).

3.2.3. CMD Analysis

There are no major issues in the CMD analysis of KMT-2023-BLG-1286. We note that by combining the t_E and ρ measurements from Table 6 with the θ_* determination from Table 2 yields Einstein-radius and proper-motion estimates of

$$\theta_E = 0.365 \pm 0.080 \text{ mas}; \quad \mu_{\text{rel}} = 9.1 \pm 2.0 \text{ mas yr}^{-1} \quad (23)$$

We find that the source is offset from the baseline object by 130 mas, so the blend is unlikely to be associated with the event. The calibrated blend magnitude is $I_b = 19.37$. To allow for the mottled background of bulge fields, we place an upper limit on the lens light $I_l > 19.1$.

3.2.4. Bayesian Analysis

For KMT-2023-BLG-1286, there are three constraints on the Bayesian analysis. First, there are the measurements of t_E from Table 6. Second, there is the measurement of θ_E from Equation (23). Finally there is the upper limit on lens light, $I_l > 19.1$, from Section 3.2.3.

The posterior distributions of the lens mass and distance are shown in Figure 12. Note, from Figure 12 (see also Section 4), that the Bayesian posteriors are nearly identical for the inner and outer solutions, while the resonant solution, which is ruled out at $\Delta\chi^2 > 100$, is shown only for completeness. The host is therefore likely to be a middle M dwarf lying in or near the Galactic bulge, orbited by a Neptune-class planet.

3.3. KMT-2023-BLG-1746

Figure 13 shows an otherwise standard 1L1S light curve with Paczyński (1986) parameters $(t_0, u_0, t_E) = (199.81, 0.045, 113 \text{ day})$, punctuated by a $\Delta t_{\text{dip}} = 1.0 \text{ day}$ dip, centered at $t_{\text{anom}} = 202.5$.

3.3.1. Heuristic Analysis

These parameters imply $\tau_{\text{anom}} = 0.024$, $u_{\text{anom}} = 0.051$, and thus

$$\alpha = 241.9^\circ; \quad s_-^\dagger = 0.975; \quad q = 7.3 \times 10^{-5}. \quad (24)$$

3.3.2. Static Analysis

The grid search on the (s, q) plane returns four solutions, whose refinements with all parameters set free are shown as the “Standard models” in Tables 7–10. This is twice as many solutions as we would normally expect. The fundamental reason for this plethora of solutions is that the dip is traced by only three observations. As can be seen in Figure 13, this degeneracy could easily have been broken if there were even one observation at about 201.8 or at about 203.2. The low effective cadence (about 1 observation per night per observatory – see Figure 13) over the anomaly derives from two factors. First, the event lies in BLG37, where the intrinsic KMT cadence is $\Gamma = (0.4, 0.3, 0.3) \text{ hr}^{-1}$ for (KMTC, KMTS, KMTA), respectively. Second, the anomaly occurred on Sept 15, when the bulge was observable for only about 4 hours per night. We will return to the issue of multiple minima below. For now, we group the four solutions into two pairs, which we call “inner/outer” and “close/wide”, respectively. We see that $\alpha \simeq 241.7^\circ$ for all four solutions while $s^\dagger \equiv \sqrt{s_+ s_-} = (0.978, 975)$ for ‘the ‘inner/outer” and “close/wide” pairs, respectively. Both α and s^\dagger are very close to the heuristic predictions. The values of q for the “close/wide” solutions are also extremely close to the prediction of Equation (24), although the “inner/outer” pair has q values that are about 40% smaller. From Figure 13, we see that the “inner/outer” pair has a set of caustic crossings over the two wings of the planetary caustic, whereas the “close/wide” pair does not. This is the reason that each of the light curves (green and cyan) of the first pair has a set of two “bumps” flanking the dip in Figure 13. One expects (or perhaps, hopes) that this implies more detailed information about ρ . However, the issue is complicated by the low cadence, and so we defer consideration of it to Section 3.3.3.

The event is unusually long ($t_E \sim 113 \text{ day}$ in the Standard model), so we expect that parallax and orbital motion may play a significant role. Hence, we conduct a parallax analysis.

3.3.3. Parallax Analysis

As can be seen from Tables 7–10, there are 16 solutions. This is twice the eight solutions that one might naively expect, namely (inner,outer,close,wide) $\times(u_0 > 0,u_0 < 0)$. The reason is that for each of these eight designations, there are two solutions, one with $\pi_{EN} > 0$ and the other with $\pi_{EN} < 0$. We designate these for example, inner(+, –), which means inner solution with $u_0 > 0$ and $\pi_{EN} < 0$.

To untangle this plethora of degenerate solutions, we first ask why this two-fold north-south degeneracy exists. From Figure 14, we see that in all four cases, (inner, outer, close, wide), the parallax contours have an elongated (“one-dimensional”, 1-D) form, and within these 1-D contours, there are two minima, one near each end of the contour. The 1-D form is extremely common in microlens parallax measurements, with the narrow direction being $\pi_{E,\parallel}$, that is, the component of $\boldsymbol{\pi}_E$ in the direction of Earth’s acceleration (toward the Sun). See Gould et al. (1994). In the present case, because the event is extremely long (so that the direction of the Sun changes substantially during the event) and because the post-peak light curve is cut off by the end of the observing season, these contours are not strictly linear.

The two minima are due to the “jerk-parallax” degeneracy (Gould 2004), so-called because the jerk (acceleration derivative) of Earth’s motion masquerades as a parallax effect. We refer the reader to Gould (2004) for the mathematical origins of this degeneracy and to Park et al. (2004) for an explicit calculation of the vector separation of the two minima on the $\boldsymbol{\pi}_E$ plane. Note in particular that the north-south degeneracy is not symmetric with respect to the x -axis, but to the direction of Earth acceleration. Thus, in all eight cases, this degeneracy has a major impact on $\boldsymbol{\pi}_E$, not only in its direction, but also its magnitude. Fortunately, however, it does not have a major impact on q or ρ , which are the parameters of most immediate physical interest.

We next turn to the (\pm) degeneracy in u_0 , which is sometimes called the “ecliptic” degeneracy (Jiang et al. 2004) because it is exact for events on the ecliptic (other than changing the sign of $(u_0, \alpha, \pi_{EN}, d\alpha/dt)$). In the present case, the event lies $> 11^\circ$ from the ecliptic, so this perfect-degeneracy limit does not even approximately apply. However, this degeneracy is also very small for high-magnification events ($u_0 \ll 1$) because, in this case, u_0 does not differ much from $-u_0$. Hence, we expect that, for example, inner(++) will be similar to inner(–+), and inner(+–) will be similar to inner(––). This expectation is qualitatively confirmed, although it completely fails for the orbital motion parameters, which are poorly measured.

In terms of the parameters that most affect the physical interpretation (q and ρ), there are basically two groups of solutions, (inner, outer) and (close, wide). For the first, $q \sim$

6×10^{-5} and $\rho \sim 5 \times 10^{-3}$, while for the second, $q \sim 1 \times 10^{-4}$ and there are only upper limits on ρ .

We first consider the (inner, outer) pair. Very often, when there is a caustic crossing, ρ is well determined. However, because of the low effective cadence, there are models that can “avoid” the caustic at the price of just a few sigma. Thus, from Figure 15, we can see that for both the $u_0 > 0$ and $u_0 < 0$ cases, ρ is well-localized at $\rho \sim 0.0055$ near the χ^2 minima, but (for all cases except inner(+,+) and inner(-,-)) suddenly “blows up” at about 2.5σ , in particular, quickly permitting values of ρ that are ~ 3 times smaller. While these solutions seem “obviously disfavored”, albeit at a low level, we should keep in mind that this corresponds to a $\Delta\chi^2$ difference that is similar to one by which the (inner, outer) models are favored over the (close, wide) models.

In order to place this issue in context, we make use of the measurement, $\theta_* = 0.65 \mu\text{as}$, from Table 2. Hence, $\rho \sim 0.005$ would imply $\theta_E \sim 0.12 \text{ mas}$ and so $\mu_{\text{rel}} \sim 0.5 \text{ mas yr}^{-1}$. For typical events, we would regard such a low proper motion as “improbable” and “suspicious”, but KMT-2023-BLG-1746 is very long ($t_E \sim 90$ day in the parallax models), and the major cause of extremely long events is low proper motion (Han et al. 2018). Moreover, Gould (2022) showed that planetary events that enter our sample are strongly biased toward low proper motion relative to their rate in nature. Another aspect is that with $\theta_E \sim 0.12 \text{ mas}$ and $\pi_E \geq |\pi_{E,E}| \gtrsim 0.10$, the lens would have $\pi_{\text{rel}} = \theta_E \pi_E \gtrsim 0.012$, which would allow it be in the bulge. This would naturally account for the direction of $\boldsymbol{\pi}_E$ (same as the direction of $\boldsymbol{\mu}_{\text{rel}}$) in the negative East direction ($\pi_{E,E} < 0$). This direction is more difficult (though by no means impossible) to accommodate for disk lenses. In this case, $M = \theta_E / \kappa \pi_E \lesssim 0.15 M_\odot$, so the lens could be a late M dwarf in the bulge.

By contrast, the (close, wide) solutions favor much lower $\rho \lesssim (0.001, 0.002)$ at 1σ , although they do accommodate $\rho \sim 0.005$ at 3σ . That is, it is very likely that they are disk lenses. Hence, if late-time imaging (taken when the lens and source had separated) showed a proper motion $\mu_{\text{rel}} \sim 0.5 \text{ mas yr}^{-1}$, then the (inner, outer) solutions would be strongly favored. Of course, even with the advent of the EELT with a FWHM $\sim 14 \text{ mas}$ in K -band, this would require a wait time of several decades. On the other hand, if the proper motion were measured at $\mu_{\text{rel}} \gtrsim 1.5 \text{ mas yr}^{-1}$, then the (close, wide) solutions would be strongly favored.

3.3.4. CMD Analysis

Recall that for this event, there are 16 separate solutions, four in each of the four

topologies that we have labeled “inner”, “outer”, “close” and “wide”. From the standpoint of the θ_E and μ_{rel} measurements, the first two topologies (“inner” and “outer”) are qualitatively different from the latter two because they have well defined ρ measurements rather than upper limits. We focus first on the best solution, inner(−+), which is described in Table 7. By combining the t_E and ρ measurements from that table with the θ_* determination from Table 2, we obtain the Einstein-radius and proper-motion estimates for this solution.

$$\theta_E = 0.127 \pm 0.013 \text{ mas}; \quad \mu_{\text{rel}} = 0.499 \pm 0.052 \text{ mas yr}^{-1}, \quad (u_0 < 0) \quad (25)$$

The values for the other 7 inner+outer solutions are very similar and can be obtained from Tables 7 and 8 by the usual scaling relations. This value of μ_{rel} would be low for a randomly chosen microlensing event ($p \sim 0.04\%$), but we should keep in mind three factors. First, as shown by Gould (2022), the distribution of proper motions for planetary events (with measured proper motions) is weighted toward low proper motions by a factor $\sim \mu_{\text{rel}}^{-1}$ relative to the underlying population of events (that is, $p \rightarrow 0.4\%$). While Gould (2022) does not comment on the reason for this, probably it is that low-proper-motion events are more likely to enter the sample because lower proper motions imply more slowly evolving events that, in turn, allow ρ to be measured. Second, Han et al. (2018) have shown that a major cause of long- t_E events (in the present case, $t_E \sim 90$ d) is low proper motion. Finally, half the solutions for this event (that is, all eight of the close+wide solutions) have only an upper limit on ρ (and so only a lower limit on μ_{rel}).

We calculate the blend light, I_b , by subtracting the measured source flux from the OGLE-III baseline magnitude $I_{\text{base}} = 18.64$ to obtain $I_b = 19.4$. Unfortunately, the OGLE-III V -band baseline measurement is not precise enough to obtain a reliable blend color. To take account of the mottled background of bulge fields, we place a more conservative limit on lens light, $I_l > 19.1$.

3.3.5. Bayesian Analysis

The Bayesian analysis of KMT-2023-BLG-1746 is broadly similar to that of KMT-2023-BLG-0164, although in this case there are 16 solutions, rather than four. For this event, we also have four constraints, although they are not exactly the same as for KMT-2023-BLG-0164. The constraints on t_E , and π_E are incorporated in exactly the same way. We also handle the constraint on ρ in exactly the same way. This is essential for the eight close+wide solutions, for which (as in the case of KMT-2023-BLG-0164) there are only upper limits on ρ . In principle, we could treat the four inner solutions as “measurements” (as we did for KMT-2023-BLG-1286), and this would also be basically appropriate for the four outer solutions. However, we choose to treat all 16 solutions in a homogeneous way, and so we derive envelope functions from Figure 15. Finally, in this case, the fourth constraint is a limit on lens flux,

$I_l > 19.1$, as we discussed Section 3.3.4.

The posterior distributions of the lens mass and distance are shown in Figures 16 and 17 for the eight close/wide and eight inner/outer solutions, respectively. These posteriors demonstrate, what was already partly clear from Section 3.3.3, that the 16 solutions are broadly divided into several groups by host mass, planet mass, χ^2 , and compatibility with Galactic-model priors.

We now discuss the origins of these groupings and how the resulting degeneracies can be partly (or completely) resolved by future AO imaging.

First, as we will tabulate in Section 4, the eight inner/outer solutions are favored by $\Delta\chi^2 \sim 5$, while the eight close/wide solutions are more compatible with the Galactic-model priors. The first aspect was already clear from the tables in Section 3.3.3. The main reason for the second aspect is that the inner/outer solutions all have well-localized $\rho \sim 0.005$ determinations, whereas the close/wide solutions have only upper limits on ρ . So, at one level, the close/wide solutions appear “favored” by the Galactic-model priors simply because they can accommodate a wider variety of random realizations of these priors. More specifically, as already commented upon in Section 3.3.3, given the $\theta_* = 0.65 \mu\text{as}$ measurement from Table 2 and the $t_E \sim 90 \text{ d}$ determinations from Tables 7 and 8, the inner/outer models have $\theta_E = 0.13 \text{ mas}$ and $\mu_{\text{rel}} \sim 0.5 \text{ mas yr}^{-1}$. Such low proper motions are disfavored by Galactic models.

This same difference also explains why the inner/outer models have smaller posterior host masses. That is, with the π_E relatively constrained by Figure 14, $M = \kappa\theta_E/\pi_E = \kappa\theta_*/\pi_E\rho \propto \rho^{-1}$. Thus, a high value of ρ implies a low value of M .

Finally, q is about 1.5 times larger for the close/wide models than the inner/outer models, so $M_{\text{planet}} = qM_{\text{host}}$ is larger for the close/wide models according to the product of two independent, larger factors.

Future AO observations (almost certainly requiring EELT or other ELT) will yield a proper-motion measurement as well as a host-mass measurements, which will distinguish between the main degeneracies of the different models. For example, if the proper motion is $\mu_{\text{rel}} \sim 0.5 \text{ mas yr}^{-1}$ this will strongly favor the inner/outer models, which will in turn resolve the two-fold ambiguity in q , whereas a substantially larger μ_{rel} measurement would strongly favor the close/wide models. The same (vector) proper-motion measurement would distinguish between the $\pi_{E,N} > 0$ and $\pi_{E,N} < 0$ models. There would then remain a four-fold degeneracy, for example among the inner(−, +), inner(+, +), outer(−, +), and outer(+, +) models. However, inspection of the four tables in Section 3.3.3 shows that the differences among these are actually quite minor.

3.4. KMT-2023-BLG-0614

Figure 18 shows an otherwise standard 1L1S light curve with Paczyński (1986) parameters $(t_0, u_0, t_E) = (62.4, 0.3, 31 \text{ day})$, punctuated by a $\Delta t_{\text{bump}} = 1.5 \text{ day}$ bump, centered at $t_{\text{anom}} = 61.4$.

3.4.1. Heuristic Analysis

These parameters imply $\tau_{\text{anom}} = -0.032$, $u_{\text{anom}} = 0.3$, and thus

$$\alpha = 96^\circ; \quad s_+^\dagger = 1.16. \quad (26)$$

3.4.2. Light Curve Analysis

The grid search on the (s, q) plane returns two solutions, whose refinements with all parameters set free are shown in Table 11. We see that in the two solutions, $\alpha = (95^\circ, 96^\circ)$ while $s^\dagger \equiv \sqrt{s_+ s_-} = 1.18$, which are both very close to the heuristic predictions.

Next, we note that in both solutions $q \sim 0.01$, which is very far from the “low q ” regime that defines this paper. Nevertheless, the division of Anomaly-Finder candidates by initially-estimated q is only intended to facilitate the organization of the light-curve analyses, so we proceed with a thorough analysis of this event.

The main issue for this event is that the light curve is very well fit by a 1L2S (binary source) model. See Figure 18 and Table 11. Because the 1L2S model is slightly favored over the 2L1S models, it is unlikely that the event would be accepted into a statistical sample unless there were some other argument that significantly preferred the 2L1S interpretation.

The principal candidates for such arguments would be that the parameters of the 1L2S solution are physically implausible or that late-time imaging could yield a μ_{rel} measurement that would distinguish between the 1L2S and 2L1S solutions. As we now show, neither of these arguments is viable.

Regarding the first, in the 1L2S model, the source magnitude is $I_S = 20.7$ and the source flux ratio is $q_F = 0.015$ implying that the source companion has $I_{S,2} = 25.3$. The extinction toward this field (from the KMT web site, ultimately from Gonzalez et al. 2012) is $A_I = 2.49$. Thus, approximately, $(I_S, I_{S,2})_0 \sim (18.2, 22.8)$, corresponding to an early G dwarf and a middle M dwarf. M dwarf companions to G dwarfs are very common. For example, see Table 7 from Duquennoy & Mayor (1991). If the 1L2S model returned the normalized source radii of both sources, this might in principle contradict the expected ratio $\rho_2/\rho_1 \sim 0.3$. However, from Table 11, only ρ_2 is measured.

Regarding the second potential argument, a future μ_{rel} measurement is very unlikely to distinguish between the models in favor of 2L1S. The normalized source size is related to proper motion by $\rho_i = \theta_{*,i}/(\mu_{\text{rel}}t_{\text{E},i})$. From Table 11, the values of t_{E} are ~ 1.5 times larger for 2L1S compared to 1L2S. Hence, if we adopt $\theta_{*,2,1\text{L}2\text{S}}/\theta_{*,2\text{L}1\text{S}} \sim 0.35$, then a given (future) μ_{rel} measurement will predict a value of ρ that is half as big for the 1L2S model as for the 2L1S model.

From Figure 19, we see that if the future μ_{rel} measurement corresponded to any value of ρ for 2L1S that was within the 2.5σ range (that is, $\rho_{2\text{L}1\text{S}} < 0.03$), then it would predict a value in the range $\rho_{1\text{L}2\text{S}} < 0.015$ for 1L2S, all of which are acceptable at $\Delta\chi^2 < 3$. Hence, the 2L1S solution could not be confirmed even at marginal confidence. (Parenthetically, we note that if 1L2S were correct, and its best fit $\rho_{1\text{L}2\text{S}} \sim 0.025$ were inferred from a future μ_{rel} measurement, then the corresponding $\rho_{2\text{L}1\text{S}} \sim 0.05$ for the 2L1S case, would be ruled out at high confidence. See Figure 19. However, this does not change the fact that the planetary interpretation could not be confirmed by such a measurement.)

3.4.3. CMD Analysis

There are no OGLE-III catalogs at the position of KMT-2023-BLG-0614, so we conduct the CMD analysis in the instrumental KMTC pyDIA system. The KMTC V -band data are too noisy to yield a measurement of V_s (and hence of $(V - I)_s$). As a result, our estimate of $(V - I)_{s,0}$ in Table 2 is based on the fact that I_s is 4.9 ± 0.3 mag below the clump, implying $M_{I,s} \sim 5$, an early K dwarf.

3.4.4. Bayesian Analysis

As discussed in Section 3.4.2, this is not a secure planetary event due to a competing 1L2S solution. Therefore, we do not carry out a Bayesian analysis.

3.5. KMT-2023-BLG-1593

Figure 20 shows an otherwise standard 1L1S light curve with Paczyński (1986) parameters $(t_0, u_0, t_{\text{E}}) = (136.9, 0.25, 29 \text{ day})$, superposed by a $\Delta t_{\text{bump}} = 1.4$ day bump, centered at $t_{\text{anom}} = 140.65$.

3.5.1. Heuristic Analysis

These parameters imply $\tau_{\text{anom}} = 0.129$, $u_{\text{anom}} = 0.281$, and thus

$$\alpha = 62.7^\circ; \quad s_+^\dagger = 1.15. \quad (27)$$

3.5.2. Light Curve Analysis

The grid search on the (s, q) plane returns two solutions, whose refinements with all parameters set free are shown in Table 12. We see that $\alpha = (63^\circ, 62^\circ)$ in the solutions, while $s^\dagger \equiv \sqrt{s_+ s_-} = 1.15$, which are both extremely close to the heuristic predictions.

Next, we note that in both solutions $q \sim 0.003$, which is roughly a factor 20 higher than the “low q ” regime that defines this paper. Nevertheless, as we noted in Section 3.4.2 the division of Anomaly-Finder candidates by q is only intended to facilitate the organization of the light-curve analyses, so we proceed with a thorough analysis of this event.

As in the case of KMT-2023-BLG-0614, there is a 1L2S model that is a good fit to the data. The argument that this degeneracy is very unlikely to be resolved is very similar to the one given in Section 3.4.2 for KMT-2023-BLG-0614. Therefore, we only sketch this argument, with a focus on making explicit the small differences relative to the argument just given.

First, from Table 12, the 2L1S model is actually preferred over 1L2S by $\Delta\chi^2 = 6$. This is not sufficient to rule out the 1L2S model by itself, but it does mean that if an additional argument of modest significance could be found, it might be sufficient to push the planetary interpretation “over the threshold”.

However, going through a similar calculation, the extinction is $A_I = 3.01$, and so the dereddened magnitudes of the binary source are $(I_S, I_{S,2})_0 \sim (18.2, 23.1)$, that is, again an early G dwarf and middle M dwarf, which are common.

Again, if there were a future μ_{rel} measurement, the ratio of the inferred normalized source radii would be $\rho_{2,1L2S}/\rho_{2L1S} \sim 0.5$. Then, from Figure 21, if a μ_{rel} measurement led to the conclusion that ρ_{2L1S} were anywhere within the 2.5σ range (that is, $\rho_{2L1S} < 0.025$), the corresponding value for the 1L2S model would be $\rho_{2L1S} < 0.0125$, which would be consistent at the 1σ level. In brief, it does not appear possible to rule out (or even argue strongly against) the 1L2S model.

3.5.3. CMD Analysis

There are no OGLE-III catalogs at the position of KMT-2023-BLG-1593, so we conduct the CMD analysis in the instrumental KMTC pyDIA system. The KMTC V -band data are too noisy to yield a measurement of V_s (and hence of $(V - I)_s$). As a result, our estimate of $(V - I)_{s,0}$ in Table 2 is based on the fact that I_s is 4.26 ± 0.12 mag below the clump, implying $M_{I,s} \sim 4.15$, an early G dwarf.

3.5.4. Bayesian Analysis

As discussed in Section 3.5.2, this is not a secure planetary event due to a competing 1L2S solution. Therefore, we do not carry out a Bayesian analysis.

4. Physical Parameters

In Table 13, we show the posterior estimates and uncertainties for M_{host} , M_{planet} , D_L , and a_{\perp} for the three secure planetary systems. We also highlight specific quotable results for each case.

5. Summary

We have analyzed all of the 2023 events that were flagged by AnomalyFinder as having preliminary mass-ratio estimates $q < 2 \times 10^{-4}$ and were not already published. After eliminating false alarms due to data artifacts, five events remained, of which three proved to be unambiguous low- q planetary systems and the remaining two had ambiguous interpretations as possible single-lens binary-source (1L2S) events. All three of the former indeed have low mass ratios, KMT-2023-BLG-0164 ($q \sim 1.3 \times 10^{-4}$), KMT-2023-BLG-1286 ($q \sim 1.9 \times 10^{-4}$), and KMT-2023-BLG-1746 ($q \sim 8 \times 10^{-5}$). For the first of these, the planet host is a nearby ($D_L \sim 1.5$ kpc) star, which is either the very bright ($I = 16.0$) blend that dominates the light along the line of sight or is a binary companion to this star. This ambiguity in host mass can be resolved by future high-resolution imaging, which will probably require two epochs of EELT observations. Future high-resolution imaging will also be required to distinguish between the two groups of solutions for KMT-2023-BLG-1746, which differ in mass ratio by a factor ~ 1.5 .

This research has made use of the KMTNet system operated by the Korea Astronomy and Space Science Institute (KASI) at three host sites of CTIO in Chile, SAAO in South Africa, and SSO in Australia. Data transfer from the host site to KASI was supported by the Korea Research Environment Open NETwork (KREONET). This research was supported by KASI under the R&D program (project No. 2025-1-830-05) supervised by the Ministry of Science and ICT. W.Z. and H.Y. acknowledge support by the National Natural Science Foundation of China (Grant No. 12133005). H.Y. acknowledges support by the China Postdoctoral Science Foundation (No. 2024M762938). W.Zang acknowledges the support from the Harvard-Smithsonian Center for Astrophysics through the CfA Fellowship. J.C.Y. acknowledges support from U.S. NSF Grant No. AST-2108414 and U.S. NASA Grant No.

80NSSC25K7146. Work by C.H. was supported by the grants of National Research Foundation of Korea (2019R1A2C2085965 and 2020R1A4A2002885). J.C.Y. acknowledges support from a Scholarly Studies grant from the Smithsonian Institution. S.D. is supported by the National Natural Science Foundation of China (Grant No. 12133005). This work is supported by the China Manned Space Program with grant no. CMS-CSST-2025-A16. S.D. acknowledges the New Cornerstone Science Foundation through the XPLOER PRIZE. Y.H. was supported by the National Natural Science Foundation of China under grant No. 12422303. The OGLE project has received funding from the Polish National Science Centre grant OPUS-28 2024/55/B/ST9/00447 to AU.

REFERENCES

- Alard, C. & Lupton, R.H., 1998, *ApJ*, 503, 325
- Albrow, M.D. Michaeldalbrow/Pydia: InitialRelease On Github., vv1.0.0, Zenodo
- Albrow, M. D., Horne, K., Bramich, D. M., et al. 2009, *MNRAS*, 397, 2099
- An, J.H., Albrow, M.D., Beaulieu, J.-P. et al. 2002, *ApJ*, 572, 521
- Batista, V., Beaulieu, J.-P., Gould, A., et al. 2014, *ApJ*, 780, 54
- Batista, V., Beaulieu, J.-P., Bennett, D.P., et al. 2015, *ApJ*, 808, 170
- Bennett, D.P., Rhie, S.H., Nikolaev, S. et al. 2010, *ApJ*, 713, 837
- Bennett, D.P., Bhattacharya, A., Anderson, J., et al. 2015, *ApJ*, 808, 169
- Bennett, D. P., Bhattacharya, A., Beaulieu, J. P., et al. 2020, *AJ*, 159, 68
- Bennett, D. P., Bhattacharya, A., Beaulieu, J. P., et al. 2024a, *AJ*, 168, 15
- Bennett, D. P., Bhattacharya, A., Beaulieu, J. P., et al. 2024b, arXiv:2412.03651
- Bensby, T. Yee, J.C., Feltzing, S. et al. 2013, *A&A*, 549, A147
- Bessell, M.S., & Brett, J.M. 1988, *PASP*, 100, 1134
- Bhattacharya, A., Beaulieu, J.-P., Bennett, D.P., et al. 2019, *AJ*, 156, 289
- Bhattacharya, A., Bennett, D.P., Beaulieu, J.-P., et al. 2021, *AJ*, 162, 60
- Bond, I.A., Bennett, D.P., Sumi, T. et al. 2017, *MNRAS*, 469, 2434

- Bressan, A., Marigo, P., Girardi, L., et al. 2012, MNRAS, 427, 127
- Dong, S., Gould, A., Udalski, A., et al. 2009, ApJ, 695, 970
- Dressler, A., Bigelow, B., Hare, T., et al. 2011, PASP, 123, 901, 288
- Duquenois, A., & Mayor, M. 1991, A&A, 248, 485
- Gaia Collaboration, Vallenari, A., Brown, A.G.A., et al., 2023, A&A, 674, A1
- Gaudi, B.S. 1998, ApJ, 506, 533
- Gonzalez, O. A., Rejkuba, M., Zoccali, M., et al. 2012, A&A, 543, A13
- Gould, A. 1992, ApJ, 392, 442
- Gould, A. 2000, ApJ, 542, 785
- Gould, A. 2004, ApJ, 606, 319
- Gould, A. 2022, arXiv:2209.12501
- Gould, A., Miralda-Escudé, J. & Bahcall, J.N. 1994, ApJ, 423, L105
- Griest, K. & Hu, W. 1992, ApJ, 397, 362
- Han, C. & Gould, A. 1997, ApJ, 480, 196
- Han, C., Jung, Y.K., Shvarzvald, Y. 2018, AJ, 865, 14
- Han, C., Udalski, A., Lee, C.-U., et al. 2024a, A&A, 683A, 187
- Han, C., Bond, I.A., Udalski, A., et al. 2024b, A&A, 687A, 241
- Han, C., Bond, I.A., Jung, Y.K., et al. 2025a, A&A, 694A, 90
- Han, C., Albrow, M.D., Lee, C.-U., et al. 2025b, AJ, 169, 288
- Huang, Y., Beers, T. C., Wolf, C., et al. 2022, ApJ, 925, 164
- Hwang, K.-H., Zang, W., Gould, A., et al. 2022, AJ, 163, 43
- Jiang, G., DePoy, D.L., Gal-Yam, A., et al. 2004, ApJ, 617, 307
- Jung, Y. K., Han, C., Udalski, A., et al. 2021, AJ, 161, 293
- Jung, Y. K., Zang, W., Han, C., et al. 2022, AJ, 164, 262

- Jung, Y. K., Zang, W., Wang., H., et al. 2023, *AJ*, 165, 226
- Kervella, P., Thévenin, F., Di Folco, E., & Ségransan, D. 2004a, *A&A*, 426, 297
- Kervella, P., Bersier, D., Mourard, D., et al. 2004b, *A&A*, 428, 587
- Kim, S.-L., Lee, C.-U., Park, B.-G., et al. 2016, *JKAS*, 49, 37
- Kim, H.-W., Hwang, K.-H., Shvartzvald, et al. 2018, arXiv:1806.07545
- Marigo, P., Girardi, L., Bressan, A., et al. 2017, *ApJ*, 835, 77
- Nataf, D.M., Gould, A., Fouqué, P. et al. 2013, *ApJ*, 769, 88
- Paczyński, B. 1995, *Acta Astron.*, 45, 345
- Paczyński, B. 1986, *ApJ*, 304, 1
- Park, B.-G., DePoy, D.L., Gaudi, B.S., et al. 2004, *ApJ*, 609, 166
- Poindexter, S., Afonso, C., Bennett, D.P., et al. 2005, *ApJ*, 633, 914
- Reksini, N.E., Batista, V., Ranc, C., et al. 2024, *AJ*, 167, 145
- Reksini, N.E., Ranc, C., Koshimoto, N. et al. 2025, arXiv:2502.12942
- Ryu, Y.-H., Jung, Y.K., Yang, H., et al. 2022, *AJ*, 164, 180
- Ryu, Y.-H., Shin, I.-G., Yang, H., et al. 2023, *AJ*, 165, 83
- Sánchez-Blázquez, P., Peletier, R. F., Jiménez-Vicente, J., et al. 2006, *MNRAS*, 371, 703
- Shvartzvald, Y., Yee, J.C., Calchi Novati, S. et al. 2017, *ApJ*, 840, L3
- Smith, M., Mao, S., & Paczyński, B., 2003, *MNRAS*, 339, 925
- Szymański, M.K., Udalski, A., Soszyński, I., et al. 2011, *Acta Astron.*, 61, 83
- Terry, S.K., Bhattacharya, A., Bennett, D.P., et al. 2021, *AJ*, 161, 54
- Terry, S.K., Beaulieu, J.-P., Bennett, D.P., et al. 2024, *AJ*, 168, 72
- Tomaney, A.B. & Crofts, A.P.S. 1996, *au*, 112, 2872
- Vandorou, A., Bennett, D.P., Beaulieu, J.-P., et al. 2020, *AJ*, 160, 121
- Yang, H., Yee, J.C., Hwang, K.-H., et al. 2024, *MNRAS*, 528, 11

Yee, J.C., Shvartzvald, Y., Gal-Yam, A. et al. 2012, ApJ, 755, 102

Yoo, J., DePoy, D.L., Gal-Yam, A. et al. 2004, ApJ, 603, 139

Zang, W., Hwang, K.-H., Udalski, A., et al. 2021, AJ, 162, 163

Zang, W., Yang, H., Han, c., et al. 2022, MNRAS, 515, 928

Zang, W., Jung, Y.K., et al. 2024, Science,

Zhang, K., Gaudi, B.S., Bloom, J.S, 2021, arXiv:2111.13696

Table 1. EVENT NAMES, OBSERVATIONAL CADENCES, ALERTS, AND LOCATIONS

Name	Γ (hr ⁻¹)	Alert Date	RA _{J2000}	Dec _{J2000}	l	b
KMT-2023-BLG-0164	2.4	27 Mar 2023	17:59:11.98	-31:46:14.41	-0.95	-3.96
OGLE-2023-BLG-0116	0.1					
MOA-2023-BLG-107	1.2					
KMT-2023-BLG-1286	4.0	19 Jun 2023	18:05:28.46	-27:52:11.32	+3.12	-3.23
OGLE-2023-BLG-0803	1.0					
KMT-2023-BLG-1746	0.4	19 Jul 2023	17:48:38.60	-35:17:53.09	-5.11	-3.84
KMT-2023-BLG-0614	2.0	28 Apr 2023	17:57:19.04	-27:55:27.19	+2.19	-1.69
KMT-2023-BLG-1593	4.0	10 Jul 2023	17:54:34.33	-28:24:47.12	+1.46	-1.42

Note. — The coordinates given here are for the nearest catalog stars (i.e., baseline objects).

Table 2. CMD PARAMETERS FOR FIVE 2023 PLANET CANDIDATES

Parameter	KB230164	KB231286	KB231746	KB230614	KB231593
$(V - I)_s$	2.22±0.02	1.61±0.04	1.44±0.01	N.A.	N.A.
$(V - I)_{cl}$	2.50±0.02	1.86±0.03	1.81±0.03	3.28±0.04	3.65±0.05
$(V - I)_{cl,0}$	1.06	1.06	1.06	1.06	1.06
$(V - I)_{s,0}$	0.78±0.03	0.81±0.05	0.69±0.03	0.90±0.10	0.70±0.10
I_s	19.49±0.03	20.38±0.05	19.40±0.05	21.79±0.31	21.41±0.11
I_{cl}	16.18±0.04	15.30±0.05	15.66±0.05	16.90±0.05	17.15±0.05
$I_{cl,0}$	14.50	14.35	14.62	14.37	14.38
$I_{s,0}$	17.81±0.05	19.43±0.07	18.36±0.07	19.26±0.31	18.64±0.12
θ_* (μ as)	0.922±0.054	0.447±0.036	0.653±0.045	0.550±0.113	0.580±0.071

Note. — Event names are abbreviations, e.g., KMT-2023-BLG-0164. $[(V - I), I]_s$ and $[(V - I), I]_{cl}$ for KB230164, KB231286, and KB231746 are based on calibrated OGLE-III photometry, while the other two events have instrumental KMT photometry.

Table 3. STANDARD MODELS FOR KMT-2023-BLG-0164

Parameters	inner	outer
χ^2/dof	6129.514/6080	6180.430/6080
$t_0 - 2460050$	1.237 ± 0.012	1.231 ± 0.013
u_0	0.074 ± 0.002	0.072 ± 0.002
t_E (days)	73.409 ± 1.473	75.855 ± 1.506
s	0.861 ± 0.004	0.968 ± 0.005
q (10^{-4})	1.321 ± 0.153	0.946 ± 0.118
$\log q$ (mean)	-3.880 ± 0.050	-4.024 ± 0.054
α (rad)	3.575 ± 0.003	3.572 ± 0.003
$\rho[2\sigma, 3\sigma]$ (10^{-4})	[< 54, < 76]	[< 62, < 81]
I_S [OGLE]	19.495 ± 0.026	19.539 ± 0.026
I_B [OGLE]	15.885 ± 0.001	15.883 ± 0.001

Table 4. PARALLAX + ORBITAL MOTION MODELS FOR KMT-2023-BLG-0164

Parameters	inner(-)	outer(-)	inner(+)	outer(+)
χ^2/dof	6075.949/6077	6075.277/6077	6078.749/6077	6078.442/6077
$t_0 - 2460050$	1.211 ± 0.016	1.214 ± 0.016	1.211 ± 0.015	1.212 ± 0.015
u_0	-0.078 ± 0.002	-0.078 ± 0.002	0.076 ± 0.002	0.076 ± 0.002
t_E (days)	69.546 ± 1.434	69.554 ± 1.401	73.258 ± 1.593	73.405 ± 1.635
s	$0.867^{+0.020}_{-0.025}$	$1.083^{+0.037}_{-0.019}$	$0.879^{+0.017}_{-0.022}$	$1.080^{+0.027}_{-0.018}$
q (10^{-4})	$1.457^{+0.646}_{-0.437}$	$0.954^{+0.842}_{-0.261}$	$1.154^{+0.470}_{-0.329}$	$0.977^{+0.540}_{-0.347}$
$\log q$ (mean)	-3.839 ± 0.150	-3.974 ± 0.184	-3.940 ± 0.142	-4.006 ± 0.178
α (rad)	2.720 ± 0.065	$2.647^{+0.114}_{-0.037}$	$3.611^{+0.048}_{-0.062}$	$3.635^{+0.060}_{-0.077}$
$\rho[2\sigma, 3\sigma]$ (10^{-4})	[< 7, < 32]	[< 1.7, < 2.3]	[< 5, < 48]	[< 1.3, < 2.0]
$\pi_{E,N}$	0.705 ± 0.094	0.723 ± 0.087	0.507 ± 0.071	0.524 ± 0.064
$\pi_{E,E}$	0.145 ± 0.039	0.155 ± 0.037	0.155 ± 0.039	0.164 ± 0.036
ds/dt (yr^{-1})	-0.316 ± 0.458	$-3.770^{+0.387}_{-0.623}$	-0.473 ± 0.423	$-3.632^{+0.392}_{-0.515}$
$d\alpha/dt$ (yr^{-1})	0.448 ± 2.023	$2.764^{+1.134}_{-3.562}$	$-0.271^{+1.925}_{-1.442}$	$-0.958^{+2.343}_{-1.837}$
I_S [OGLE]	19.443 ± 0.027	19.444 ± 0.026	19.470 ± 0.028	19.471 ± 0.028
I_B [OGLE]	15.886 ± 0.001	15.886 ± 0.001	15.885 ± 0.001	15.885 ± 0.001
β	$0.206^{+0.307}_{-0.160}$	0.431 ± 0.235	$0.262^{+0.302}_{-0.199}$	0.425 ± 0.236

Table 5. PARALLAX TEST FOR KMT-2023-BLG-0164

Observatory	$\pi_{E,N}$	$\pi_{E,E}$	Corr.Coeff	χ^2
KMTC	0.391 ± 0.153	0.026 ± 0.078	0.919	5.70
Complement	0.384 ± 0.159	0.134 ± 0.076	0.890	
KMTS	0.430 ± 0.221	0.161 ± 0.109	0.890	2.41
Complement	0.407 ± 0.127	0.064 ± 0.063	0.910	
KMTA	0.219 ± 0.280	0.059 ± 0.121	0.903	1.63
Complement	0.434 ± 0.121	0.083 ± 0.062	0.908	
OGLE	0.652 ± 0.436	0.288 ± 0.252	0.869	0.76
Complement	0.404 ± 0.114	0.078 ± 0.056	0.908	

Table 6. MICROLENS PARAMETERS FOR KMT-2023-BLG-1286

Parameters	inner	outer	resonant	1L2S
χ^2/dof	9482.396/9483	9483.132/9483	9591.802/9483	9589.705/9483
$t_0 - 2460110$	8.787 ± 0.014	8.787 ± 0.014	8.582 ± 0.018	8.820 ± 0.016
u_0	0.132 ± 0.006	0.132 ± 0.006	0.111 ± 0.004	0.152 ± 0.007
t_E (days)	14.705 ± 0.467	14.677 ± 0.458	17.387 ± 0.511	13.874 ± 0.480
s	1.116 ± 0.004	1.025 ± 0.004	0.999 ± 0.001	...
q (10^{-4})	1.899 ± 0.177	1.874 ± 0.172	65.867 ± 4.685	...
$\log q$ (mean)	-3.722 ± 0.040	-3.727 ± 0.040	-2.180 ± 0.032	...
α (rad)	1.729 ± 0.008	1.729 ± 0.008	3.185 ± 0.017	...
ρ (10^{-3})	1.225 ± 0.250	1.214 ± 0.269	1.531 ± 0.095	...
$t_{0,2} - 2460110$	8.477 ± 0.001
$u_{0,2}$ (10^{-4})	$1.123^{+1.009}_{-0.722}$
ρ_2 (10^{-3})	1.132 ± 0.070
q_F (10^{-3})	2.731 ± 0.130
I_S [OGLE]	20.415 ± 0.049	20.412 ± 0.049	20.660 ± 0.044	20.291 ± 0.056
I_B [OGLE]	19.579 ± 0.021	19.581 ± 0.021	19.493 ± 0.014	19.641 ± 0.029
$I_{S,2}$ [OGLE]	26.704 ± 0.065
t_* (hours)	$0.432^{+0.079}_{-0.097}$	0.428 ± 0.094	0.637 ± 0.028	...
$t_{*,2}$ (hours)	0.377 ± 0.019

Table 7. MICROLENS PARAMETERS FOR KMT-2023-BLG-1746, INNER MODELS

Parameters	Standard	Parallax + orbital motion models			
		inner(+, -)	inner(+, +)	inner(-, -)	inner(-, +)
		$u_0 > 0, \pi_{E,N} < 0$	$u_0 > 0, \pi_{E,N} > 0$	$u_0 < 0, \pi_{E,N} < 0$	$u_0 < 0, \pi_{E,N} > 0$
χ^2/dof	1193.561/1112	1109.022/1109	1109.656/1109	1109.444/1109	1109.540/1109
$t_0 - 2460190$	9.808 ± 0.024	9.911 ± 0.025	9.909 ± 0.025	9.910 ± 0.026	9.912 ± 0.025
u_0	0.044 ± 0.002	0.056 ± 0.003	0.057 ± 0.003	-0.057 ± 0.003	-0.058 ± 0.003
t_E (days)	113.674 ± 4.515	92.880 ± 3.908	90.026 ± 4.301	90.462 ± 4.163	89.889 ± 3.758
s	$0.968^{+0.004}_{-0.006}$	$0.960^{+0.007}_{-0.009}$	$0.961^{+0.007}_{-0.009}$	$0.961^{+0.007}_{-0.009}$	0.960 ± 0.008
q (10^{-5})	3.981 ± 0.647	5.670 ± 0.799	5.699 ± 0.733	5.900 ± 0.777	5.967 ± 0.865
$\log q$ (mean)	-4.399 ± 0.068	-4.245 ± 0.065	-4.246 ± 0.056	-4.231 ± 0.059	-4.223 ± 0.067
α (rad)	4.216 ± 0.005	4.244 ± 0.010	4.240 ± 0.014	2.049 ± 0.010	2.042 ± 0.011
ρ (10^{-3})	4.199 ± 0.249	5.136 ± 0.396	5.294 ± 0.424	5.295 ± 0.386	5.278 ± 0.459
$\pi_{E,N}$...	-0.196 ± 0.106	0.086 ± 0.081	-0.181 ± 0.105	0.096 ± 0.085
$\pi_{E,E}$...	-0.181 ± 0.036	-0.121 ± 0.018	-0.167 ± 0.029	-0.129 ± 0.018
ds/dt (yr^{-1})	...	$-0.603^{+1.323}_{-0.961}$	$-0.503^{+1.318}_{-1.049}$	-0.600 ± 1.172	-0.656 ± 1.113
$d\alpha/dt$ (yr^{-1})	...	0.758 ± 0.995	0.034 ± 1.716	-0.445 ± 1.199	-0.674 ± 1.345
I_S [KMTC]	19.648 ± 0.048	19.371 ± 0.054	19.356 ± 0.055	19.367 ± 0.053	19.345 ± 0.053
I_B [KMTC]	18.521 ± 0.012	18.673 ± 0.023	18.666 ± 0.024	18.673 ± 0.024	18.670 ± 0.024
t_* (hours)	$11.522^{+0.414}_{-0.609}$	$11.466^{+0.656}_{-0.834}$	11.443 ± 0.689	11.501 ± 0.604	$11.436^{+0.661}_{-0.889}$
β	...	$0.145^{+0.142}_{-0.108}$	$0.270^{+0.291}_{-0.193}$	$0.267^{+0.286}_{-0.204}$	$0.250^{+0.300}_{-0.182}$

Table 8. MICROLENS PARAMETERS FOR KMT-2023-BLG-1746, OUTER MODELS

Parameters	Standard	Parallax + orbital motion models			
		outer(+, -)	outer(+, +)	outer(-, -)	outer(-, +)
		$u_0 > 0, \pi_{E,N} < 0$	$u_0 > 0, \pi_{E,N} > 0$	$u_0 < 0, \pi_{E,N} < 0$	$u_0 < 0, \pi_{E,N} > 0$
χ^2/dof	1197.211/1112	1109.570/1109	1109.811/1109	1109.627/1109	1109.757/1109
$t_0 - 2460190$	9.813 ± 0.023	9.912 ± 0.026	9.911 ± 0.025	9.910 ± 0.026	9.912 ± 0.026
u_0	0.045 ± 0.002	0.056 ± 0.003	0.058 ± 0.003	-0.057 ± 0.003	-0.058 ± 0.003
t_E (days)	113.056 ± 4.426	93.184 ± 4.072	89.636 ± 4.276	90.539 ± 4.289	89.821 ± 3.870
s	$0.988^{+0.006}_{-0.004}$	$0.987^{+0.008}_{-0.006}$	0.985 ± 0.008	0.984 ± 0.007	0.986 ± 0.007
q (10^{-5})	4.591 ± 0.540	$5.702^{+1.116}_{-0.750}$	$6.170^{+1.076}_{-0.801}$	6.188 ± 0.805	5.914 ± 0.854
$\log q$ (mean)	-4.338 ± 0.051	-4.236 ± 0.071	-4.205 ± 0.067	-4.210 ± 0.054	-4.228 ± 0.060
α (rad)	4.218 ± 0.005	$4.255^{+0.010}_{-0.015}$	4.237 ± 0.014	2.050 ± 0.011	2.034 ± 0.012
ρ (10^{-3})	4.019 ± 0.296	$4.829^{+0.424}_{-0.623}$	$5.192^{+0.443}_{-0.577}$	5.179 ± 0.445	$5.093^{+0.407}_{-0.511}$
$\pi_{E,N}$...	-0.186 ± 0.107	0.083 ± 0.080	-0.176 ± 0.104	0.101 ± 0.087
$\pi_{E,E}$...	-0.177 ± 0.036	-0.123 ± 0.019	-0.166 ± 0.029	-0.129 ± 0.018
ds/dt (yr^{-1})	...	-0.462 ± 1.111	-0.318 ± 1.281	-0.217 ± 1.231	$-0.549^{+1.219}_{-0.954}$
$d\alpha/dt$ (yr^{-1})	...	$-0.766^{+1.794}_{-1.075}$	$0.731^{+1.565}_{-2.041}$	-0.703 ± 1.279	0.439 ± 1.513
I_S [KMTC]	19.641 ± 0.047	19.375 ± 0.056	19.350 ± 0.055	19.367 ± 0.054	19.344 ± 0.055
I_B [KMTC]	18.524 ± 0.012	18.672 ± 0.024	18.669 ± 0.024	18.673 ± 0.024	18.671 ± 0.026
t_* (hours)	$10.951^{+0.565}_{-0.765}$	$10.895^{+0.757}_{-1.446}$	$11.233^{+0.733}_{-1.179}$	$11.290^{+0.670}_{-0.918}$	$11.013^{+0.704}_{-1.009}$
β	...	0.392 ± 0.261	0.346 ± 0.248	$0.286^{+0.306}_{-0.208}$	$0.260^{+0.276}_{-0.173}$

Table 9. MICROLENS PARAMETERS FOR KMT-2023-BLG-1746, CLOSE MODELS

Parameters	Standard	Parallax + orbital motion models			
		close(+, -)	close(+, +)	close(-, -)	close(-, +)
		$u_0 > 0, \pi_{E,N} < 0$	$u_0 > 0, \pi_{E,N} > 0$	$u_0 < 0, \pi_{E,N} < 0$	$u_0 < 0, \pi_{E,N} > 0$
χ^2/dof	1205.003/1112	1115.207/1109	1115.668/1109	1114.831/1109	1115.499/1109
$t_0 - 2460190$	9.813 ± 0.023	9.916 ± 0.026	9.915 ± 0.026	9.916 ± 0.026	9.915 ± 0.026
u_0	0.044 ± 0.002	0.057 ± 0.003	0.059 ± 0.003	-0.058 ± 0.003	-0.058 ± 0.003
t_E (days)	113.582 ± 4.491	91.796 ± 4.235	87.937 ± 4.093	87.975 ± 4.335	89.729 ± 3.700
s	$0.929^{+0.006}_{-0.004}$	0.927 ± 0.008	0.926 ± 0.008	0.927 ± 0.008	0.929 ± 0.008
q (10^{-5})	7.487 ± 0.870	9.380 ± 1.157	10.059 ± 1.234	10.164 ± 1.390	9.545 ± 1.173
$\log q$ (mean)	-4.128 ± 0.049	-4.028 ± 0.052	-3.999 ± 0.053	-3.994 ± 0.057	-4.020 ± 0.051
α (rad)	4.219 ± 0.005	4.252 ± 0.010	4.242 ± 0.009	2.046 ± 0.010	2.039 ± 0.009
ρ (10^{-3})	< 3.8	< 5.2	< 6.3	< 6.2	< 6.4
$\pi_{E,N}$...	-0.234 ± 0.107	0.117 ± 0.086	-0.247 ± 0.095	0.113 ± 0.089
$\pi_{E,E}$...	-0.195 ± 0.039	-0.124 ± 0.019	-0.188 ± 0.031	-0.129 ± 0.018
ds/dt (yr^{-1})	...	$-0.551^{+0.859}_{-0.646}$	$-0.473^{+0.834}_{-0.636}$	$-0.705^{+0.913}_{-0.639}$	$-0.694^{+0.742}_{-0.583}$
$d\alpha/dt$ (yr^{-1})	...	0.053 ± 1.047	0.138 ± 0.957	$-0.315^{+1.169}_{-0.891}$	-0.435 ± 0.819
I_S [KMTC]	19.647 ± 0.048	19.355 ± 0.059	19.329 ± 0.054	19.338 ± 0.056	19.342 ± 0.052
I_B [KMTC]	18.522 ± 0.012	18.678 ± 0.025	18.675 ± 0.025	18.681 ± 0.025	18.670 ± 0.024
β	...	0.356 ± 0.251	0.354 ± 0.251	0.410 ± 0.250	0.357 ± 0.248

Table 10. MICROLENS PARAMETERS FOR KMT-2023-BLG-1746, WIDE MODELS

Parameters	Standard	Parallax + orbital motion models			
		wide(+, -)	wide(+, +)	wide(-, -)	wide(-, +)
		$u_0 > 0, \pi_{E,N} < 0$	$u_0 > 0, \pi_{E,N} > 0$	$u_0 < 0, \pi_{E,N} < 0$	$u_0 < 0, \pi_{E,N} > 0$
χ^2/dof	1204.215/1112	1113.598/1109	1114.355/1109	1114.012/1109	1114.488/1109
$t_0 - 2460190$	9.814 ± 0.023	9.917 ± 0.026	9.917 ± 0.025	9.915 ± 0.025	9.916 ± 0.026
u_0	0.045 ± 0.002	0.058 ± 0.003	0.060 ± 0.003	-0.057 ± 0.003	-0.059 ± 0.003
t_E (days)	113.322 ± 4.494	91.578 ± 4.171	86.535 ± 3.960	89.488 ± 4.271	88.877 ± 3.845
s	$1.023^{+0.005}_{-0.007}$	1.011 ± 0.008	1.010 ± 0.008	$1.016^{+0.008}_{-0.010}$	1.012 ± 0.008
q (10^{-5})	7.285 ± 0.923	9.251 ± 1.134	9.936 ± 1.241	9.823 ± 1.415	9.558 ± 1.236
$\log q$ (mean)	-4.139 ± 0.055	-4.034 ± 0.051	-4.005 ± 0.053	-4.010 ± 0.061	-4.021 ± 0.055
α (rad)	4.219 ± 0.005	4.254 ± 0.009	4.247 ± 0.008	2.046 ± 0.009	2.035 ± 0.009
ρ (10^{-3})	< 3.8	< 5.0	< 5.6	< 6.1	< 5.9
$\pi_{E,N}$...	-0.239 ± 0.105	0.142 ± 0.082	-0.212 ± 0.107	0.120 ± 0.089
$\pi_{E,E}$...	-0.198 ± 0.039	-0.124 ± 0.019	-0.177 ± 0.031	-0.132 ± 0.018
ds/dt (yr^{-1})	...	$0.634^{+0.594}_{-0.838}$	$0.578^{+0.581}_{-0.723}$	-0.105 ± 0.840	$0.266^{+0.700}_{-0.892}$
$d\alpha/dt$ (yr^{-1})	...	-0.192 ± 0.789	-0.549 ± 0.643	-0.363 ± 0.840	-0.056 ± 0.858
I_S [KMTC]	19.644 ± 0.048	19.351 ± 0.059	19.312 ± 0.053	19.356 ± 0.054	19.330 ± 0.055
I_B [KMTC]	18.523 ± 0.012	18.680 ± 0.025	18.679 ± 0.025	18.676 ± 0.024	18.676 ± 0.025
β	...	0.357 ± 0.241	0.386 ± 0.255	0.328 ± 0.252	0.356 ± 0.252

Table 11. MICROLENS PARAMETERS FOR KMT-2023-BLG-0614

Parameters	inner	outer	1L2S
χ^2/dof	6654.314/6654	6653.790/6654	6652.735/6654
$t_0 - 2460060$	2.346 ± 0.241	2.433 ± 0.249	2.670 ± 0.335
u_0	0.287 ± 0.067	$0.305^{+0.088}_{-0.069}$	0.678 ± 0.187
t_E (days)	31.823 ± 5.121	30.635 ± 5.279	$20.437^{+4.578}_{-3.026}$
s	1.470 ± 0.051	0.947 ± 0.066	...
q (10^{-2})	$1.347^{+0.373}_{-0.296}$	$1.175^{+0.331}_{-0.268}$...
$\log q$ (mean)	-1.872 ± 0.106	-1.932 ± 0.111	...
α (rad)	1.662 ± 0.026	1.670 ± 0.027	...
ρ (10^{-2})	< 3.0	< 4.0	...
$t_{0,2} - 2460060$	1.497 ± 0.057
$u_{0,2}$	0.015 ± 0.008
ρ_2 (10^{-2})	< 4.5
q_F (10^{-2})	$1.478^{+0.535}_{-0.390}$
I_S [KMTC]	21.855 ± 0.311	21.788 ± 0.346	20.718 ± 0.512
I_B [KMTC]	$18.210^{+0.012}_{-0.009}$	$18.212^{+0.015}_{-0.010}$	$18.281^{+0.064}_{-0.045}$
$I_{S,2}$ [KMTC]	25.340 ± 0.302

Table 12. MICROLENS PARAMETERS FOR KMT-2023-BLG-1593

Parameters	inner	outer	1L2S
χ^2/dof	11950.198/11947	11946.860/11947	11952.946/11947
$t_0 - 2460130$	6.903 ± 0.082	6.834 ± 0.084	6.522 ± 0.105
u_0	0.256 ± 0.023	0.242 ± 0.021	0.260 ± 0.024
t_E (days)	28.703 ± 1.814	29.591 ± 1.811	29.161 ± 1.939
s	1.371 ± 0.021	0.966 ± 0.021	...
q (10^{-3})	3.307 ± 0.502	3.215 ± 0.492	...
$\log q$ (mean)	-2.481 ± 0.066	-2.494 ± 0.066	...
α (rad)	1.105 ± 0.015	1.087 ± 0.015	...
ρ (10^{-2})	< 2.6	< 2.5	...
$t_{0,2} - 2460130$	10.577 ± 0.041
$u_{0,2}$	$0.013^{+0.003}_{-0.005}$
ρ_2 (10^{-2})	< 2.6
q_F (10^{-2})	1.162 ± 0.233
I_S [KMTC]	21.213 ± 0.117	21.285 ± 0.111	21.251 ± 0.123
I_B [KMTC]	$21.812^{+0.233}_{-0.169}$	$21.698^{+0.180}_{-0.137}$	$21.749^{+0.221}_{-0.163}$
$I_{S,2}$ [KMTC]	26.102 ± 0.202

Table 13. PHYSICAL PROPERTIES

Event Models	Physical Properties				Relative Weights	
	$M_{\text{host}} [M_{\odot}]$	$M_{\text{planet}} [M_{\oplus}]$	D_L [kpc]	a_{\perp} [au]	Gal.Mod.	χ^2
KB230164						
inner(-)	$0.29^{+0.14}_{-0.11}$	$13.98^{+6.88}_{-5.21}$	$0.97^{+0.37}_{-0.21}$	$1.19^{+0.31}_{-0.18}$	0.391	0.715
inner(+)	0.44 ± 0.22	16.75 ± 8.55	$1.16^{+0.64}_{-0.33}$	1.57 ± 0.27	1.000	0.176
outer(-)	$0.39^{+0.06}_{-0.11}$	$12.52^{+1.95}_{-3.43}$	$0.87^{+0.11}_{-0.23}$	$1.61^{+0.16}_{-0.26}$	0.000	1.000
outer(+)	0.79 ± 0.05	25.75 ± 1.57	$0.66^{+0.08}_{-0.01}$	2.12 ± 0.08	0.000	0.206
Adopted	$0.32^{+0.21}_{-0.13}$	$14.95^{+8.21}_{-6.01}$	$1.04^{+0.51}_{-0.27}$	$1.33^{+0.39}_{-0.25}$		
KB231286						
inner	$0.31^{+0.29}_{-0.18}$	$19.89^{+18.53}_{-11.07}$	$6.15^{+0.99}_{-1.35}$	2.09 ± 0.61	0.998	1.000
outer	$0.31^{+0.29}_{-0.18}$	$19.58^{+18.30}_{-10.90}$	$6.15^{+0.99}_{-1.35}$	1.92 ± 0.56	1.000	0.692
Resonant	$0.34^{+0.30}_{-0.19}$	$750.74^{+659.90}_{-418.27}$	$6.16^{+0.99}_{-1.38}$	1.97 ± 0.58	0.814	0.000
Adopted	$0.31^{+0.29}_{-0.18}$	$19.78^{+18.48}_{-11.01}$	$6.15^{+0.99}_{-1.35}$	2.02 ± 0.60		
KB231746						
inner(+, -)	$0.11^{+0.11}_{-0.04}$	$2.00^{+2.14}_{-0.78}$	7.46 ± 0.95	$1.04^{+0.75}_{-0.18}$	0.004	1.000
inner(+, +)	0.11 ± 0.03	2.05 ± 0.48	8.16 ± 0.81	1.00 ± 0.14	0.010	0.728
inner(-, -)	$0.08^{+0.03}_{-0.02}$	$1.65^{+0.67}_{-0.47}$	7.80 ± 0.84	0.93 ± 0.13	0.004	0.810
inner(-, +)	$0.12^{+0.09}_{-0.03}$	$2.31^{+1.73}_{-0.62}$	7.83 ± 0.92	$1.05^{+0.62}_{-0.17}$	0.010	0.772
outer(+, -)	$0.14^{+0.18}_{-0.07}$	$2.73^{+3.43}_{-1.31}$	$7.22^{+0.99}_{-1.27}$	$1.34^{+0.96}_{-0.39}$	0.009	0.760
outer(+, +)	$0.13^{+0.08}_{-0.04}$	$2.63^{+1.67}_{-0.74}$	7.83 ± 0.89	$1.13^{+0.58}_{-0.20}$	0.015	0.674
outer(-, -)	$0.10^{+0.05}_{-0.03}$	$1.95^{+1.10}_{-0.65}$	7.67 ± 0.88	$1.01^{+0.35}_{-0.14}$	0.004	0.739
outer(-, +)	$0.11^{+0.04}_{-0.03}$	$2.20^{+0.81}_{-0.54}$	7.99 ± 0.85	$1.07^{+0.27}_{-0.16}$	0.010	0.693
Adopted	$0.11^{+0.08}_{-0.03}$	$2.23^{+1.52}_{-0.68}$	7.78 ± 0.94	$1.06^{+0.55}_{-0.17}$		
close(+, -)	0.40 ± 0.20	12.39 ± 6.10	$4.36^{+2.17}_{-1.75}$	2.32 ± 0.64	0.182	0.045
close(+, +)	0.46 ± 0.19	15.51 ± 6.48	$4.80^{+1.78}_{-1.28}$	2.64 ± 0.61	1.000	0.036
close(-, -)	0.37 ± 0.18	12.34 ± 6.12	$3.77^{+2.30}_{-1.40}$	2.20 ± 0.57	0.167	0.055
close(-, +)	0.46 ± 0.19	14.69 ± 6.18	$4.81^{+1.78}_{-1.30}$	2.64 ± 0.62	0.896	0.039
wide(+, -)	0.40 ± 0.19	12.29 ± 5.90	$4.11^{+2.25}_{-1.61}$	2.53 ± 0.68	0.152	0.102

Table 13—Continued

Event Models	Physical Properties				Relative Weights	
	$M_{\text{host}} [M_{\odot}]$	$M_{\text{planet}} [M_{\oplus}]$	$D_{\text{L}} [\text{kpc}]$	$a_{\perp} [\text{au}]$	Gal.Mod.	χ^2
wide(+, +)	0.45 ± 0.19	15.02 ± 6.13	$4.50^{+1.78}_{-1.20}$	2.83 ± 0.62	0.956	0.070
wide(-, -)	0.39 ± 0.20	12.59 ± 6.53	4.81 ± 1.92	2.55 ± 0.72	0.270	0.083
wide(-, +)	0.45 ± 0.19	14.39 ± 6.03	$4.72^{+1.77}_{-1.27}$	2.84 ± 0.65	0.943	0.065
Adopted	0.44 ± 0.19	14.34 ± 6.30	$4.63^{+1.85}_{-1.37}$	2.70 ± 0.66		
Adopted (Total)	0.39 ± 0.23	12.72 ± 7.92	$5.03^{+2.30}_{-1.63}$	$2.54^{+0.72}_{-1.05}$		

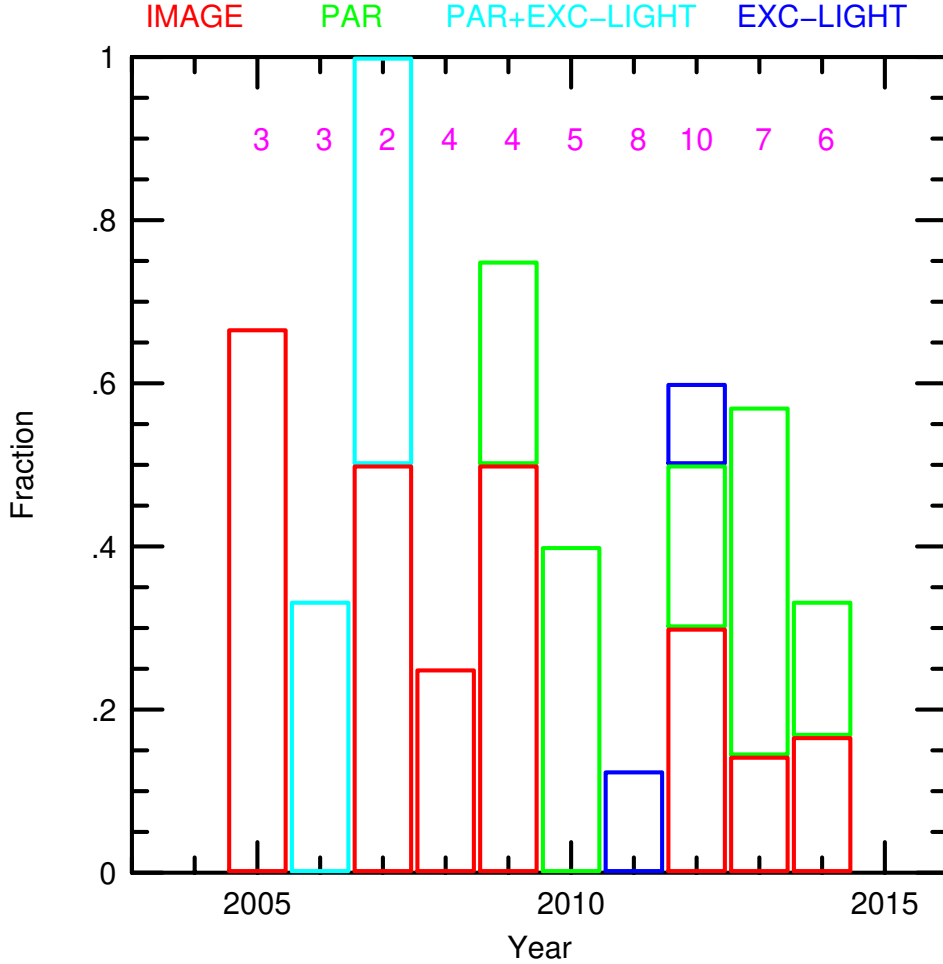


Fig. 1.— Mass-Measurements of 24 microlensing hosts for events occurring 2005-2014. The magenta numbers show the total number of planetary events for each year. The colors give the method of mass measurement, as indicated just above the image. Specifically: (1) Late-time high-resolution imaging (Batista et al. 2015; Bennett et al. 2015; Gould 2022) (“IMAGE”, red, 11); (2) Combining light-curve measurements of the microlens parallax (π_E) and Einstein radius (θ_E) to yield $M = \theta_E/\kappa\pi_E$ (Gould 1992) (“PAR”, green, 9); (3) Combining light curve measurements of π_E with excess light, relative to the source flux derived from the light curve (Bennett et al. 2010), (“PAR+EXC-LIGHT”, cyan, 2); (4) Mass derived from excess-light alone (Batista et al. 2014) (“EXC-LIGHT”, blue, 2).

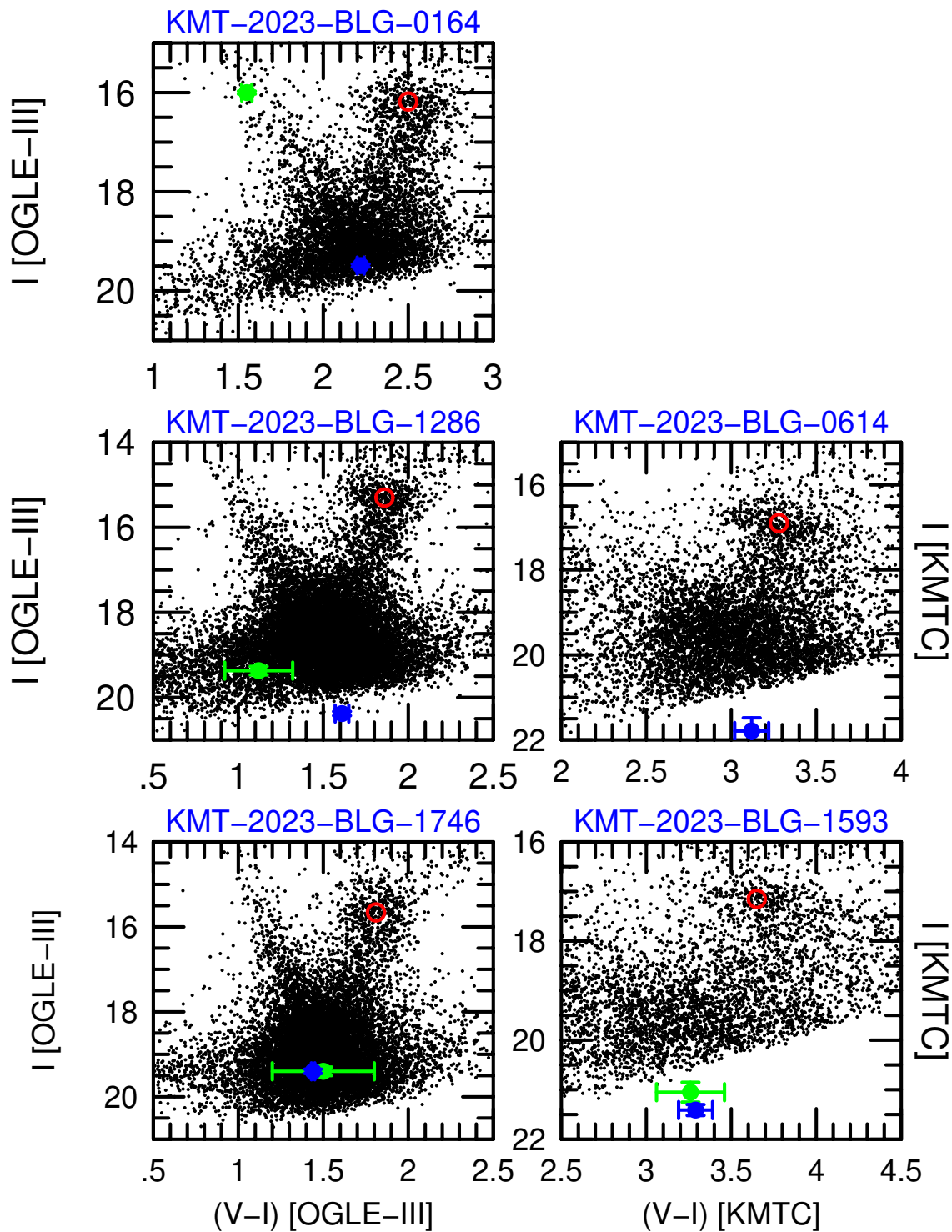


Fig. 2.— Color-magnitude diagrams (CMDs) for the five events analyzed in this paper. The positions of the source (blue), clump-giant centroid (red), and blend (green) are marked.

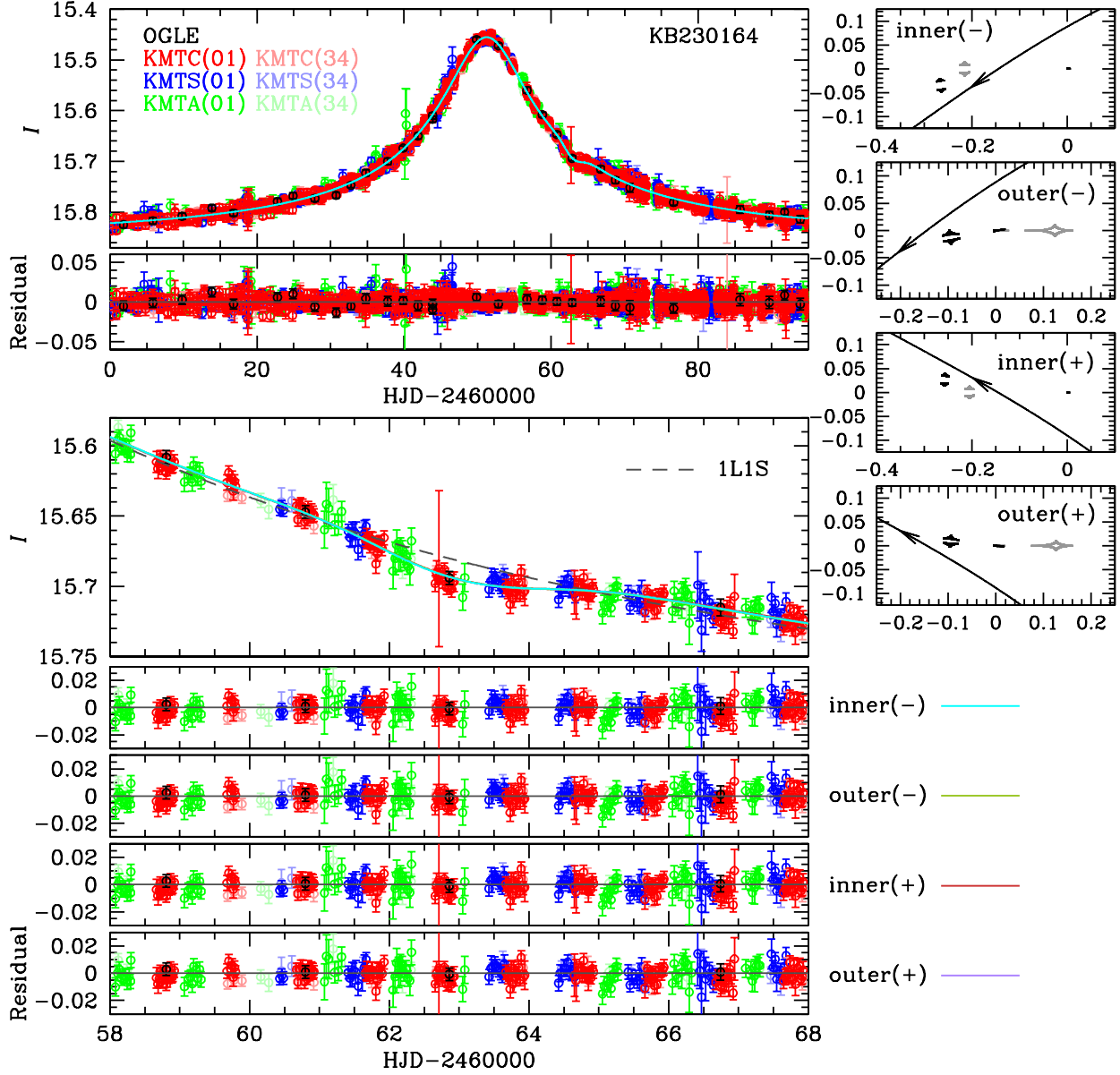


Fig. 3.— Light curve and models for KMT-2023-BLG-0164. For the four caustic-geometry insets at the right, the light-colored caustics represent the configurations at $t = t_0$, while the dark-colored caustics represent $t = t_{\text{anom}}$.

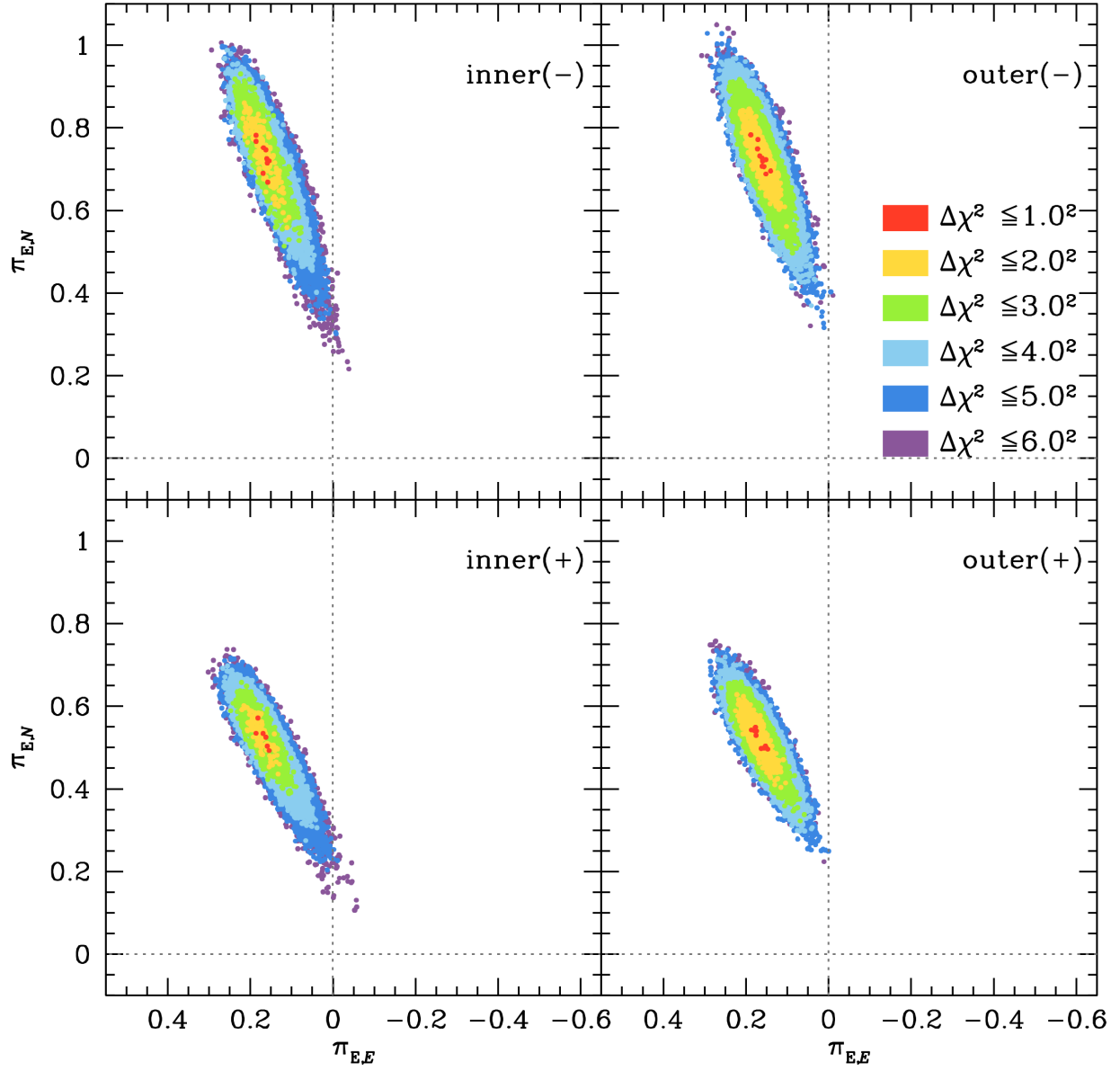


Fig. 4.— Parallax contours for the four solutions of KMT-2023-BLG-0164. Colors indicate values of $\Delta\chi^2 < 1, 4, 9, 16, 25, 36$.

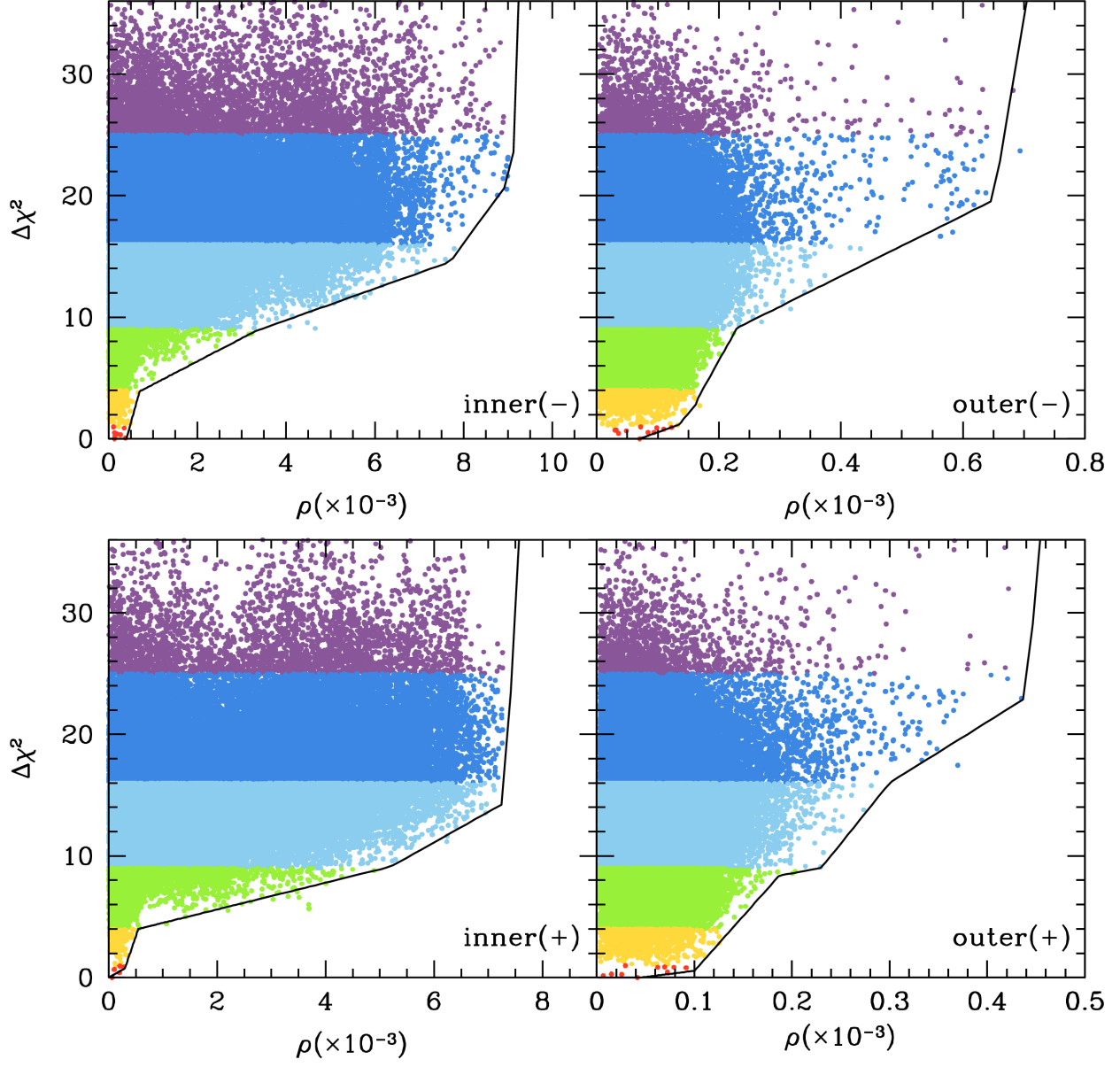


Fig. 5.— Scatter plots of the normalized source radius, ρ , against the values of $\Delta\chi^2$ relative to the best fit for each of the four solutions of KMT-2023-BLG-0164. Colors indicate values of $\Delta\chi^2 < 1, 4, 9, 16, 25, 36$. Also shown is the adopted envelope function, which is used in Section 4.

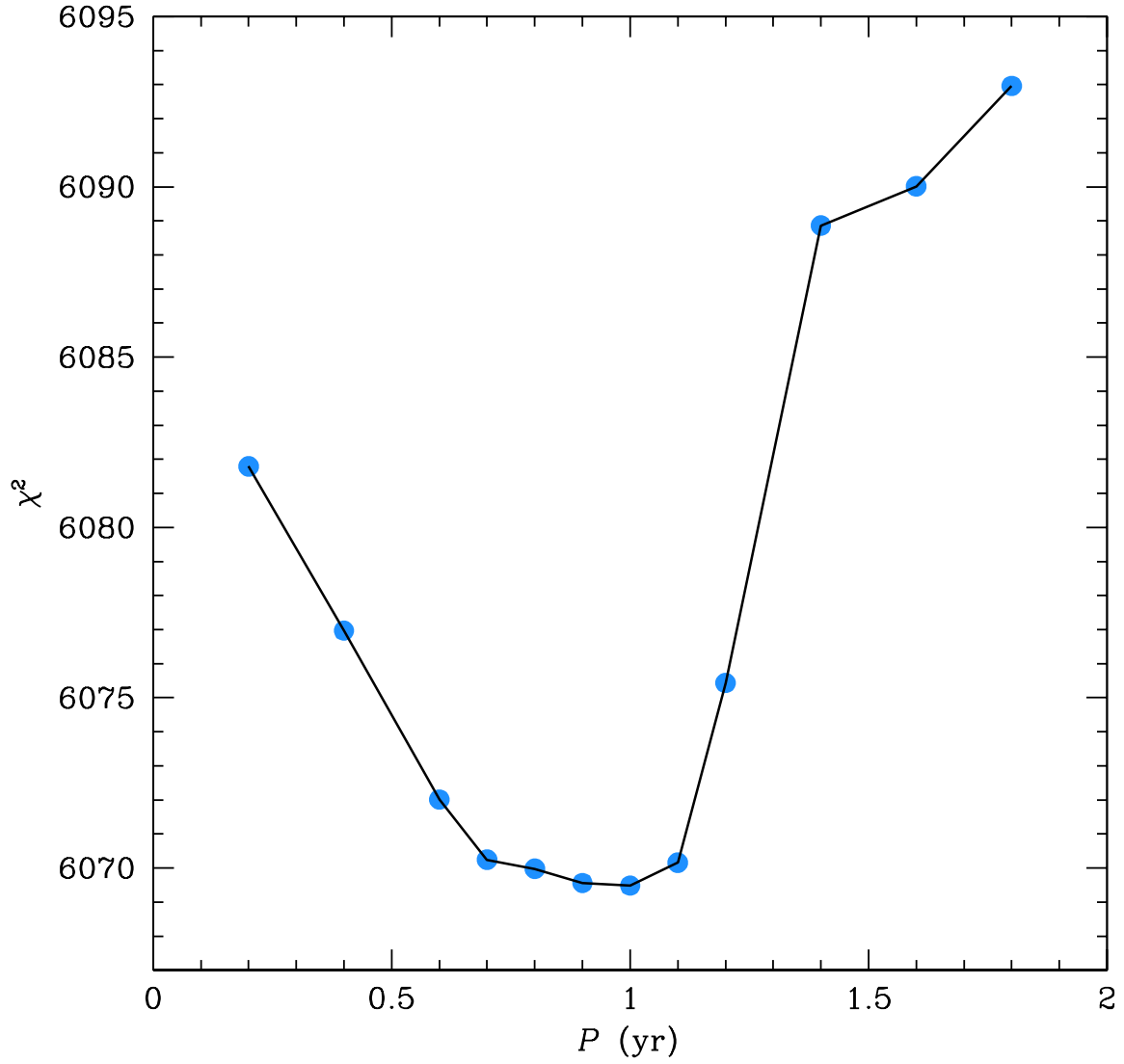


Fig. 6.— Evolution of χ^2 with assumed period P for xallarap models of KMT-2023-BLG-0164 that allow for free fits to the orientation parameters (α, δ) . The xallarap period $P = 1$ yr is the best fit, as one would expect if the actual origin of the light-curve distortion is the parallax effect induced by Earth’s annual orbital motion.

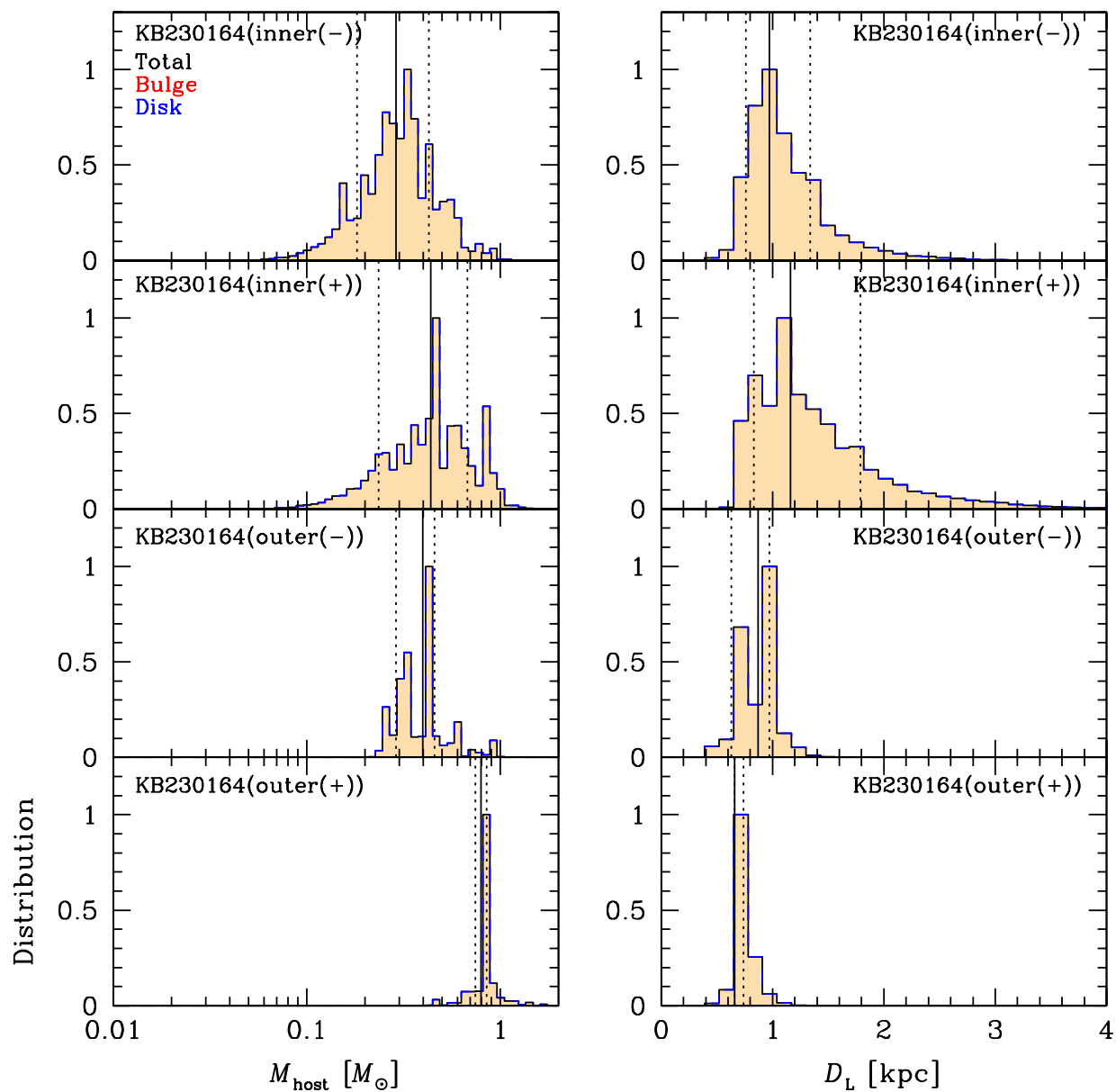


Fig. 7.— Posterior lens mass and distance distributions for the four solutions for KMT-2023-BLG-0164.

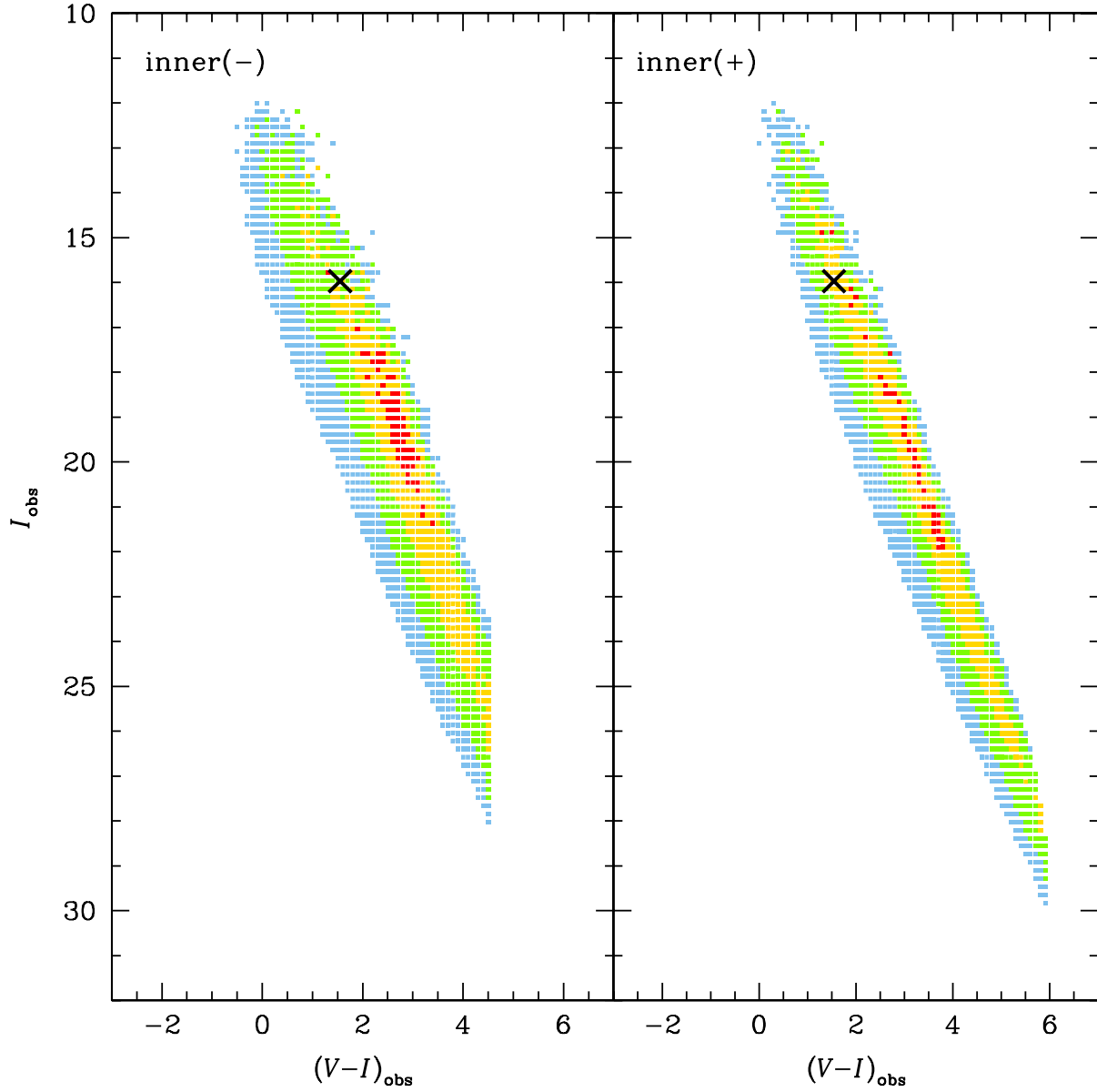


Fig. 8.— Two-dimensional color-magnitude posterior distribution for the two “inner” solutions for KMT-2023-BLG-0164. The “X” marks the position of the blend.

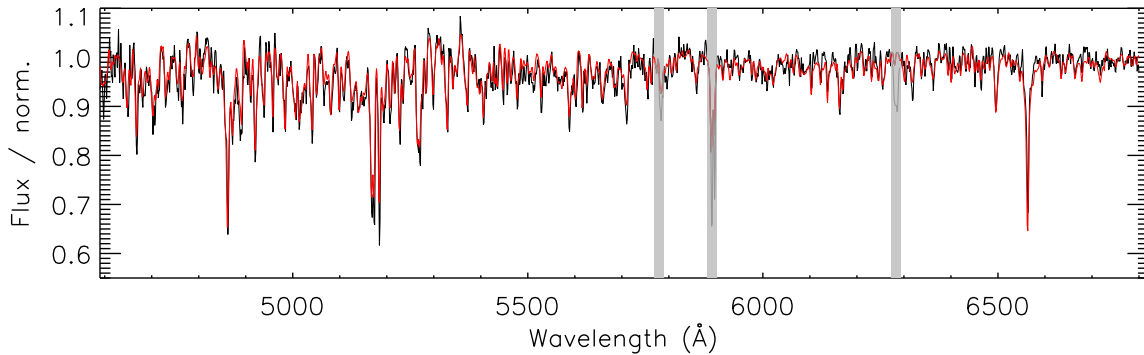


Fig. 9.— The spectrum of KMT-2023-BLG-0164 with the best-matched template. The black line shows the observed spectrum of the target obtained with IMACS, while the red line represents one of the best-matched MILES template spectrum (HD186427; $T_{\text{eff}} = 5762$ K, $\log g = 4.43$, and $[\text{Fe}/\text{H}] = 0.07$), convolved to a resolution of $R = 1000$. All spectra are continuum-normalized. The three shaded regions indicate the masked wavelength ranges affected by interstellar absorption features, including the NaID doublet and the diffuse interstellar bands (DIBs) at $\lambda\lambda 5780$ and 6283 Å.

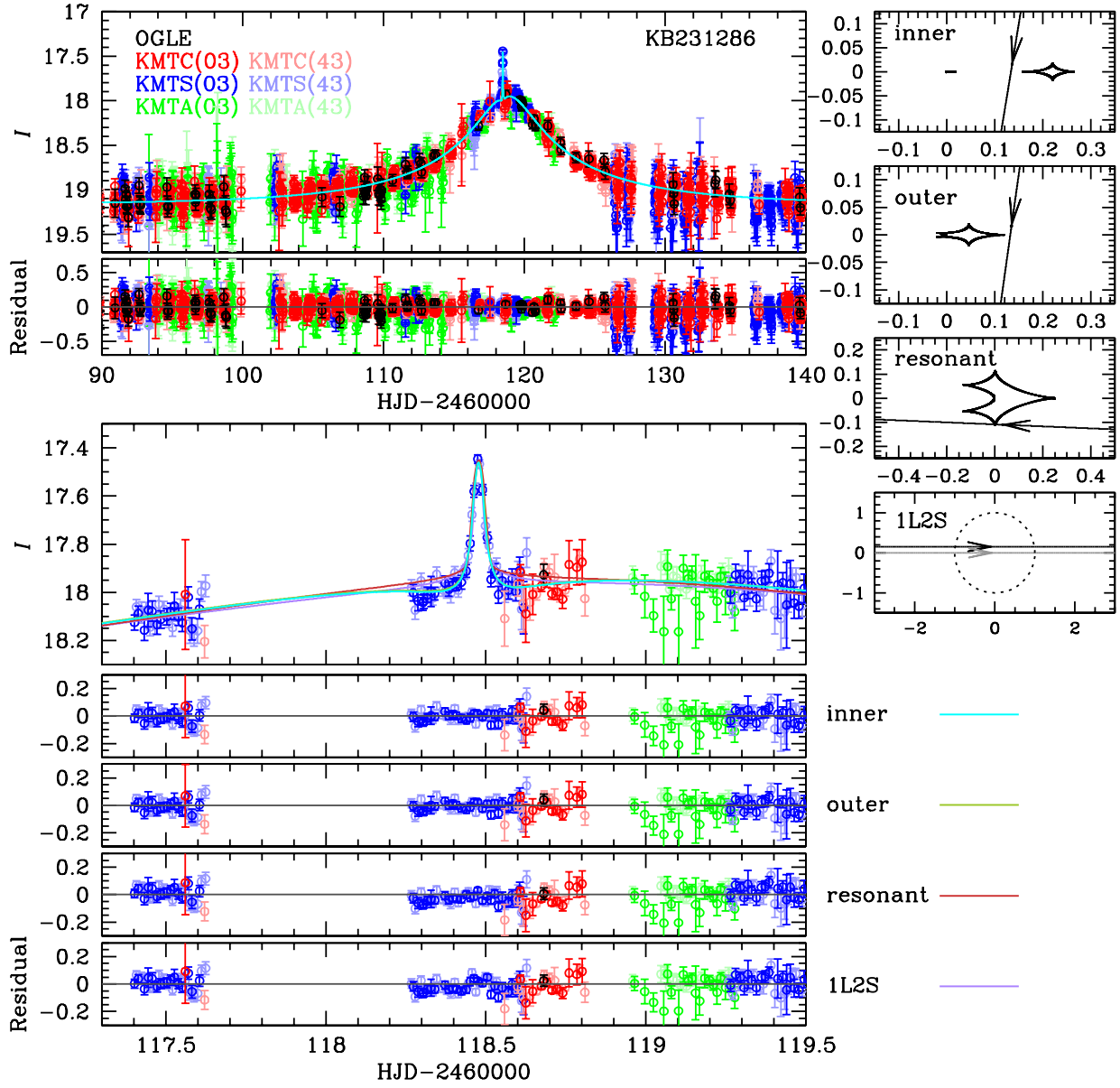


Fig. 10.— Light curve and models for KMT-2023-BLG-1286.

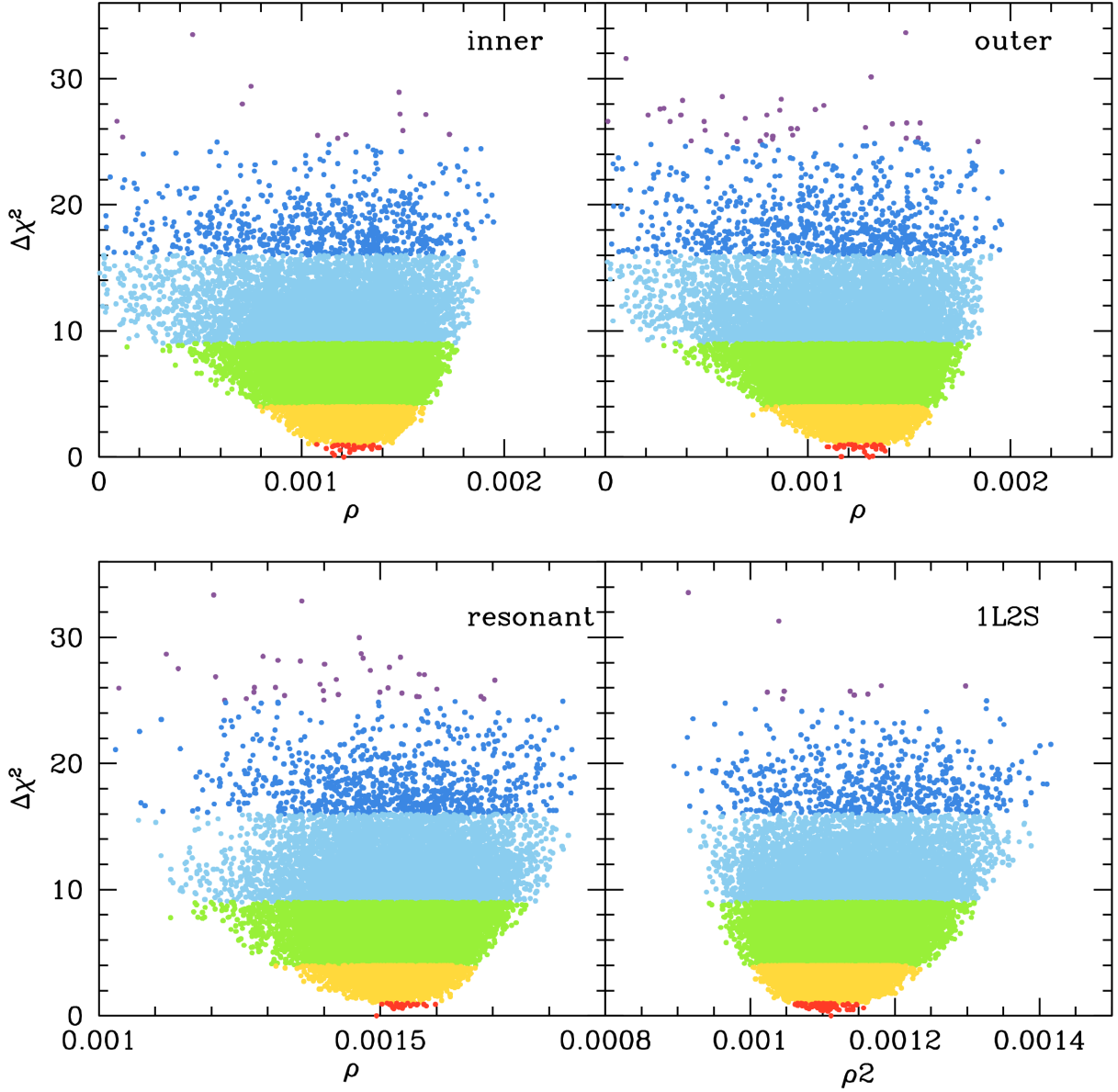


Fig. 11.— Scatter plots of the normalized source radius, ρ , against the values of $\Delta\chi^2$ relative to the best fit for each of the four tabulated solutions of KMT-2023-BLG-1286. Colors indicate values of $\Delta\chi^2 < 1, 4, 9, 16, 25, 36$.

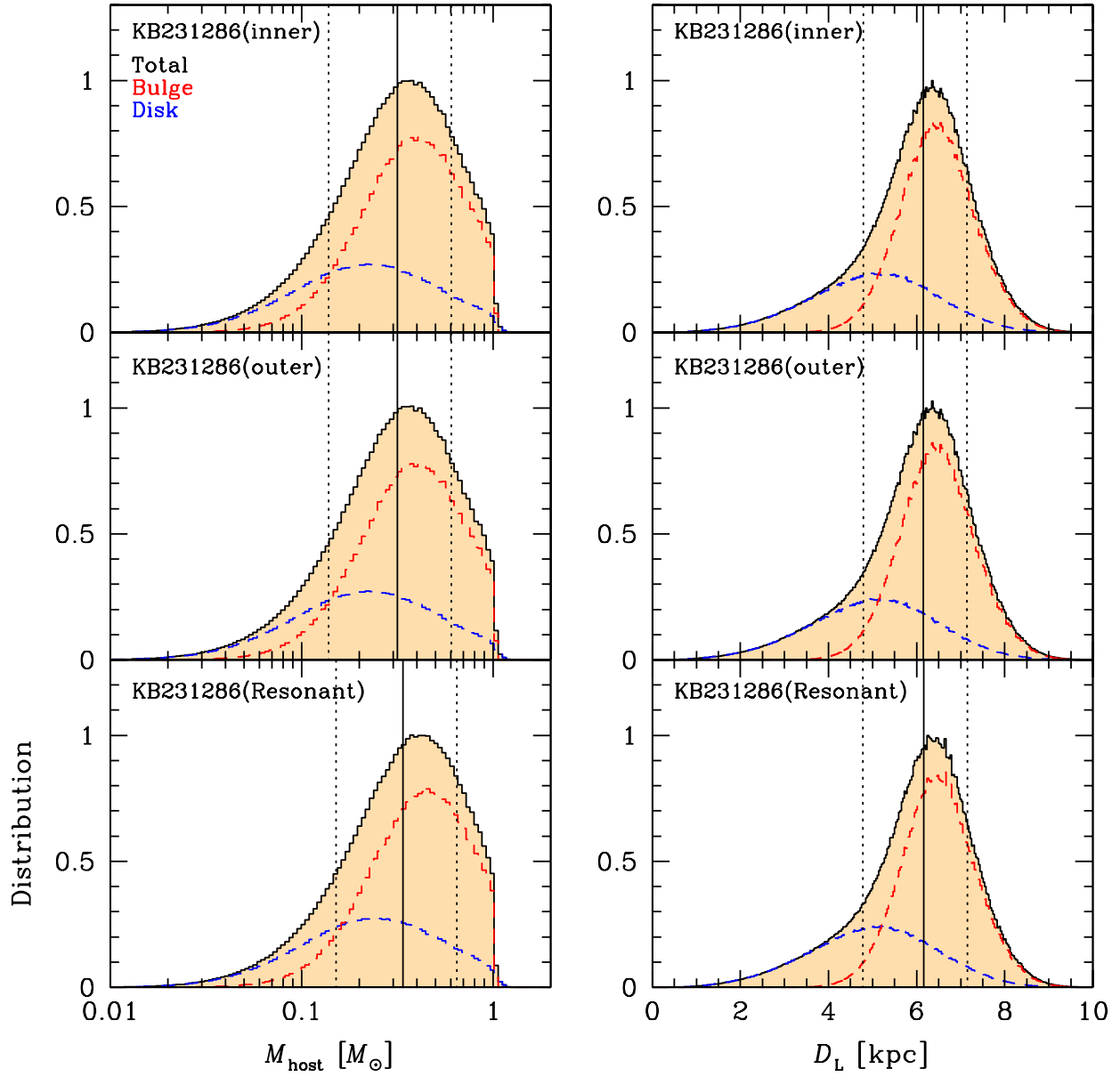


Fig. 12.— Posterior lens mass and distance distributions for the three solutions for KMT-2023-BLG-1286.

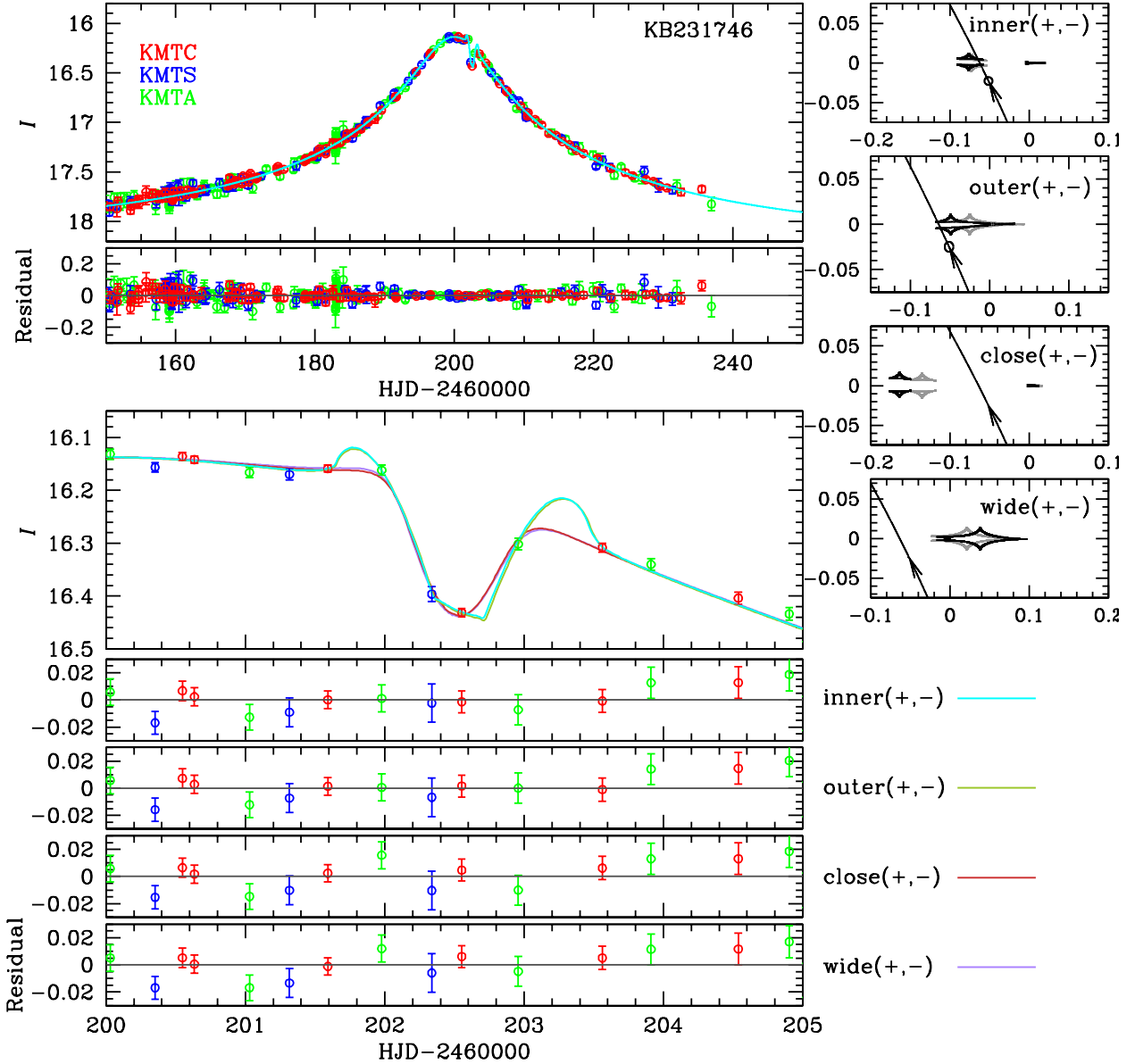


Fig. 13.— Light curve and models for the quartet of four $(+, -)$ solutions of KMT-2023-BLG-1746 with $u_0 > 0$ and $\pi_{EN} < 0$. The other three quartets look very similar and therefore are not shown explicitly. The insets to the right show the caustic geometries. Note that in the (inner, outer) pair of solutions, the source crosses the caustic, but in the (close, wide) pair, it does not. In these four panels, the light-colored caustics represent the configurations at $t = t_0$, while the dark-colored caustics represent $t = t_{\text{anom}}$.

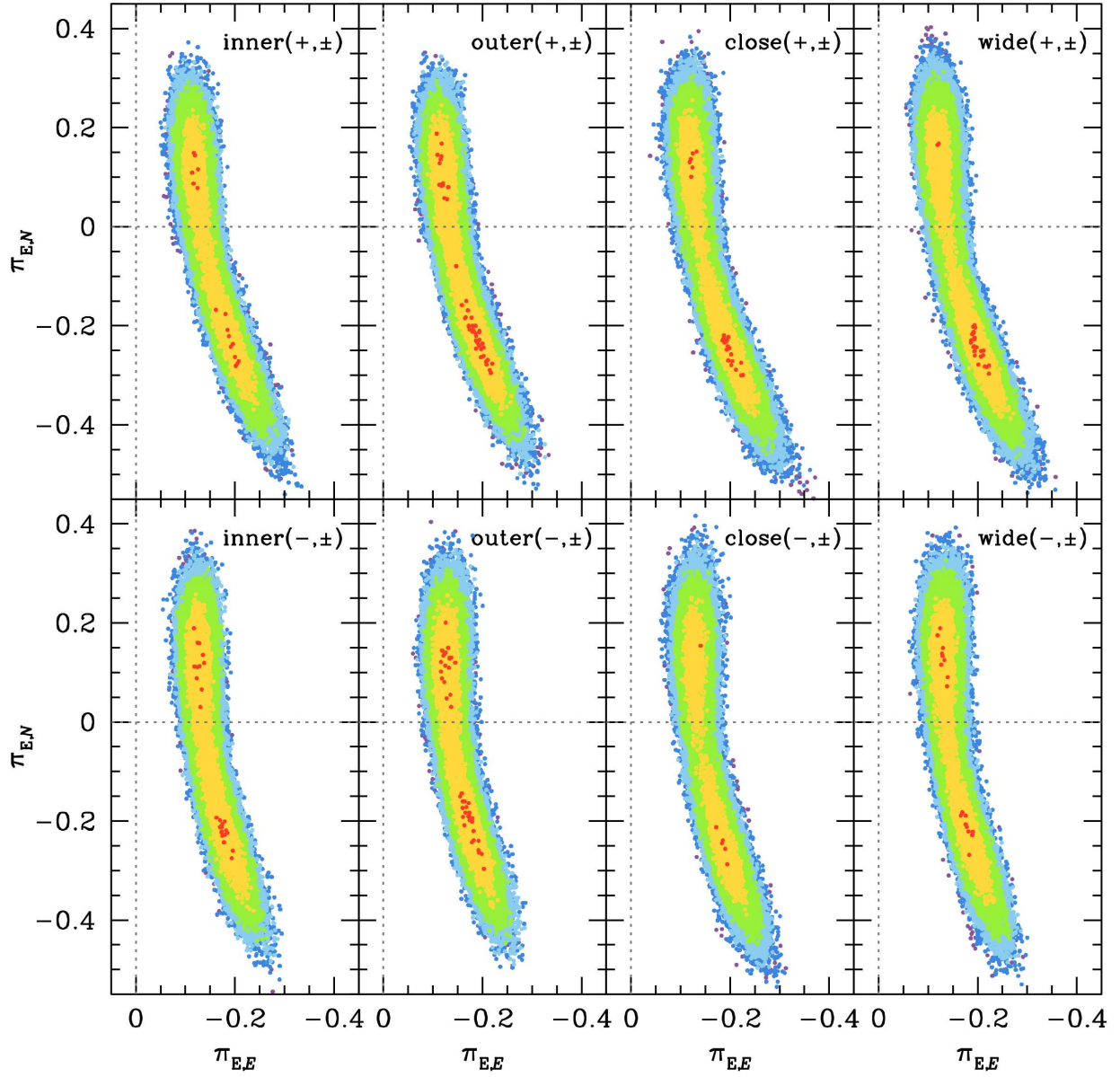


Fig. 14.— Parallax contours for the eight pairs of solutions of KMT-2023-BLG-1746. Colors indicate values of $\Delta\chi^2 < 1, 4, 9, 16, 25, 36$.

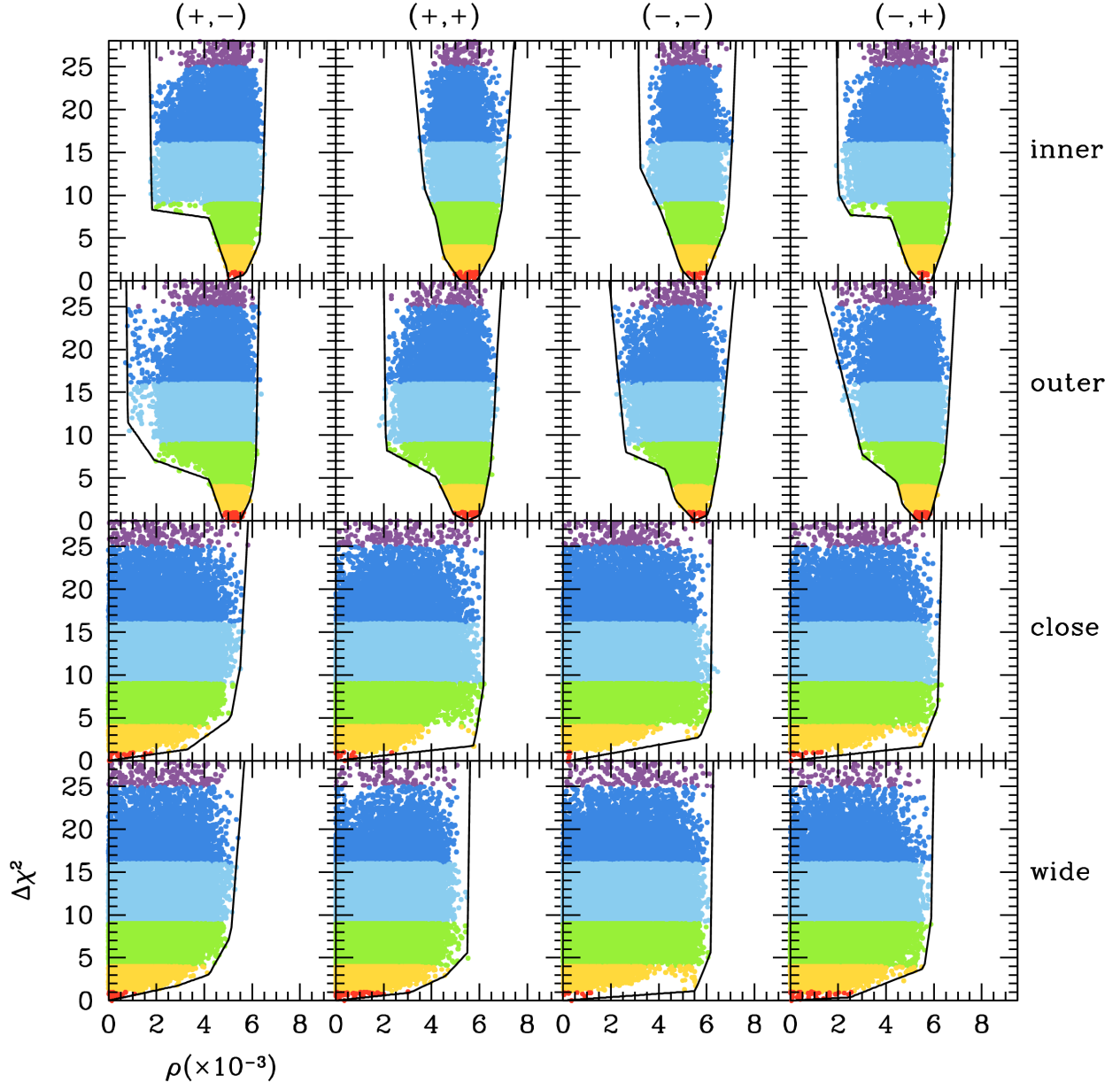


Fig. 15.— Scatter plots, for the 16 solutions of KMT-2023-BLG-1746, of the normalized source radius, ρ , against the values of $\Delta\chi^2$ relative to the best fit. Colors indicate values of $\Delta\chi^2 < 1, 4, 9, 16, 25, 36$. Also shown is the adopted envelope function, which is used in Section 4.

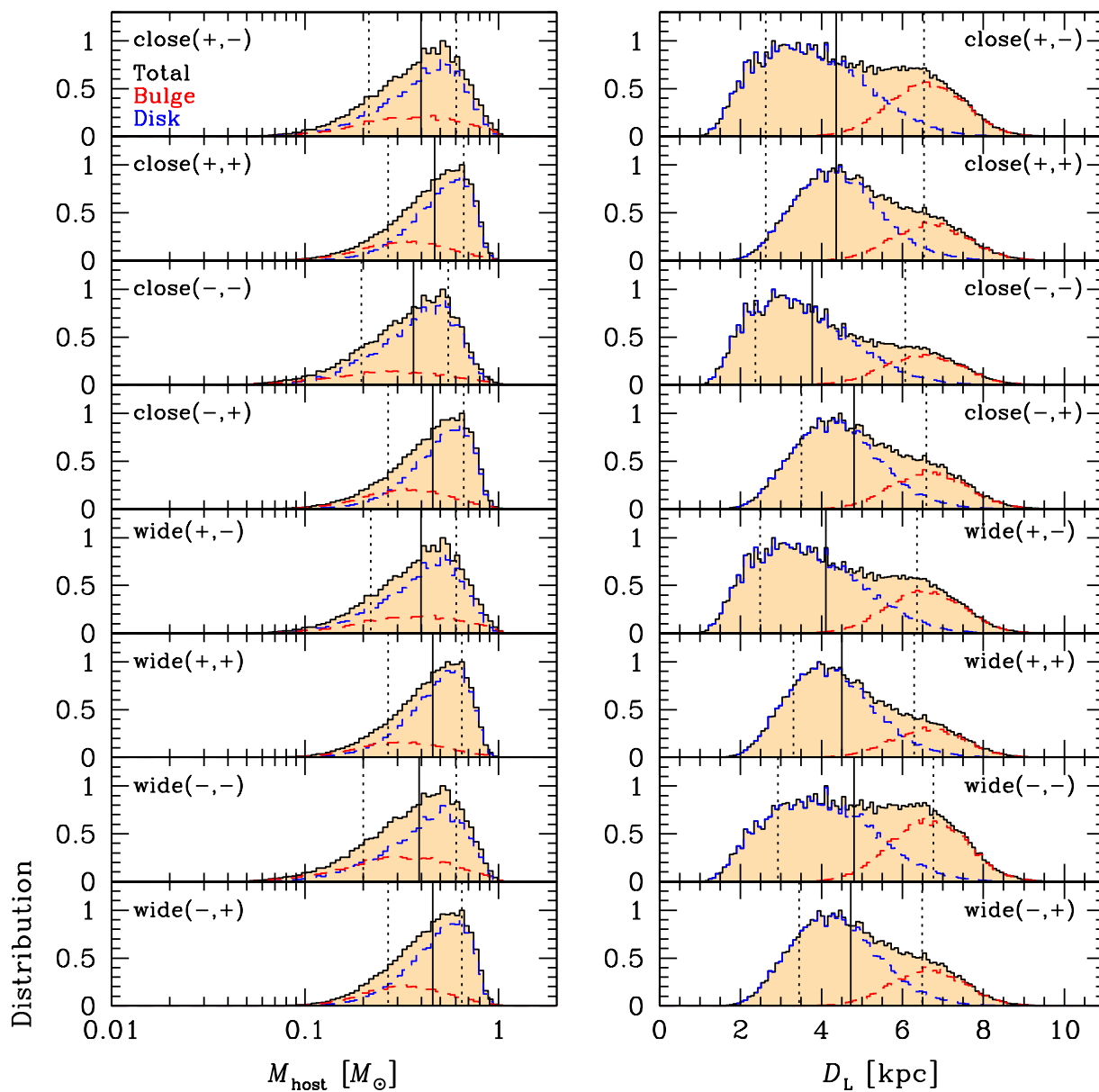


Fig. 16.— Posterior lens mass and distance distributions for the eight close/wide solutions for KMT-2023-BLG-1746.

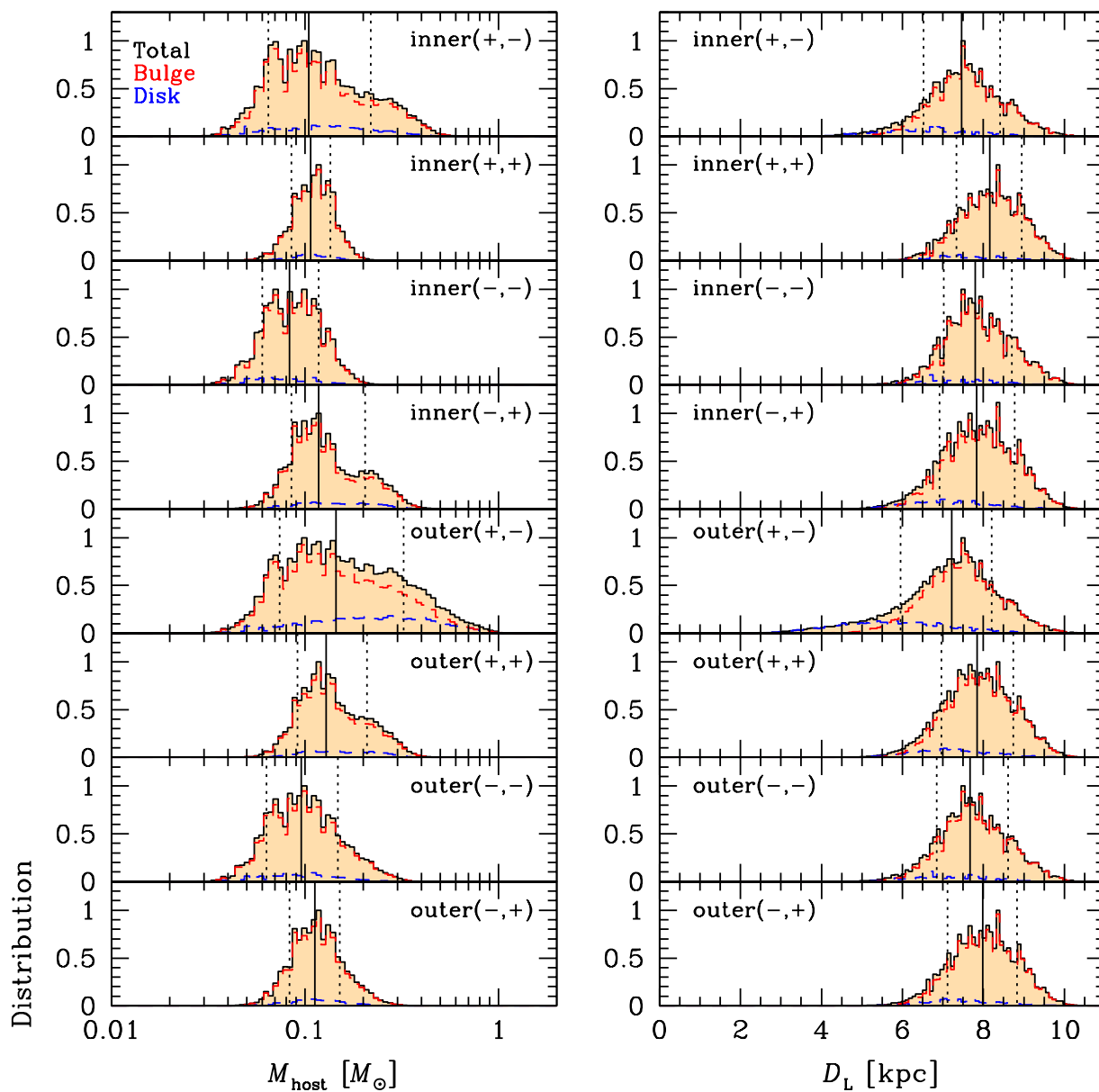


Fig. 17.— Posterior lens mass and distance distributions for the eight inner/outer solutions for KMT-2023-BLG-1746.

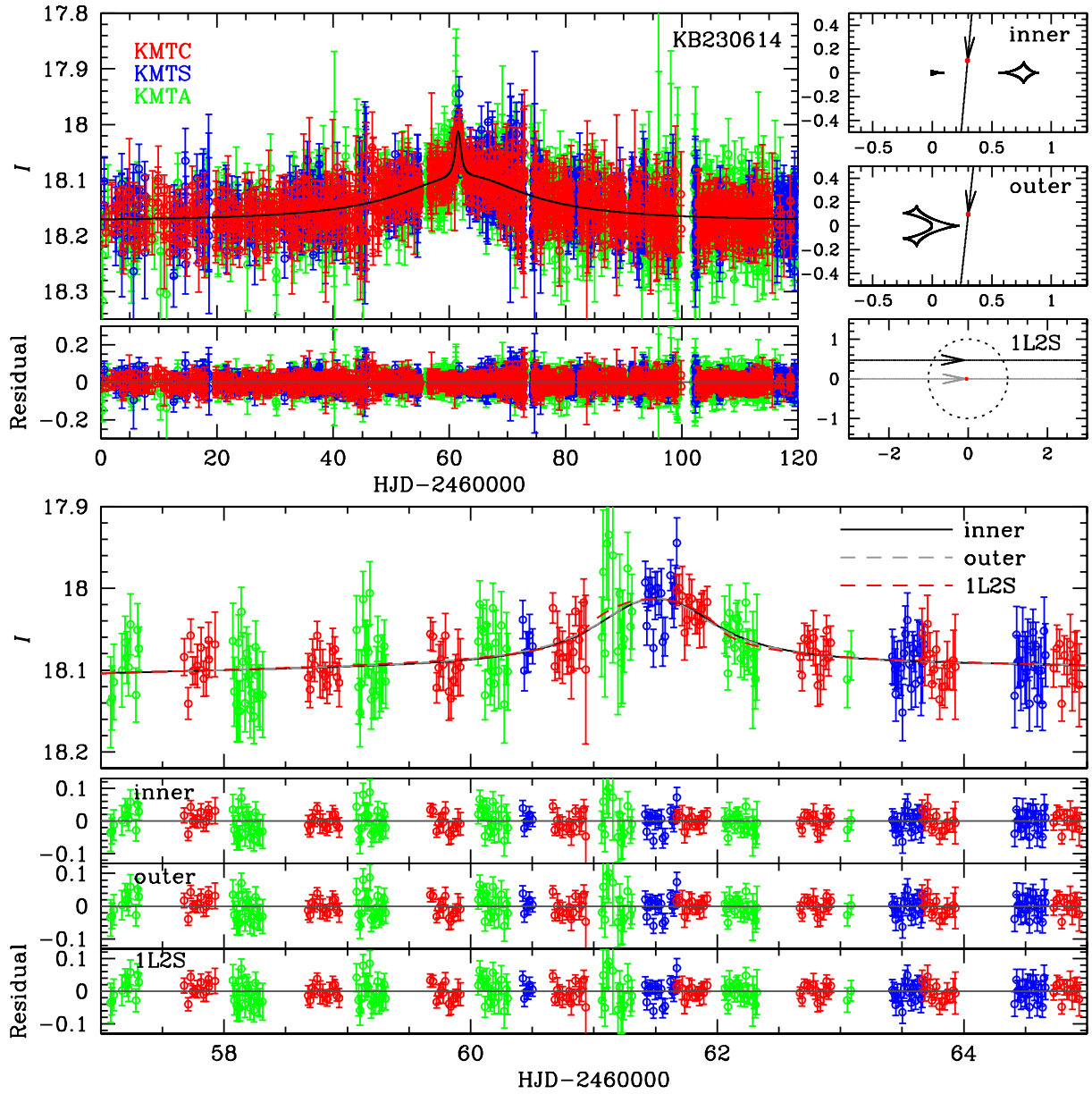


Fig. 18.— Light curve and models for KMT-2023-BLG-0614.

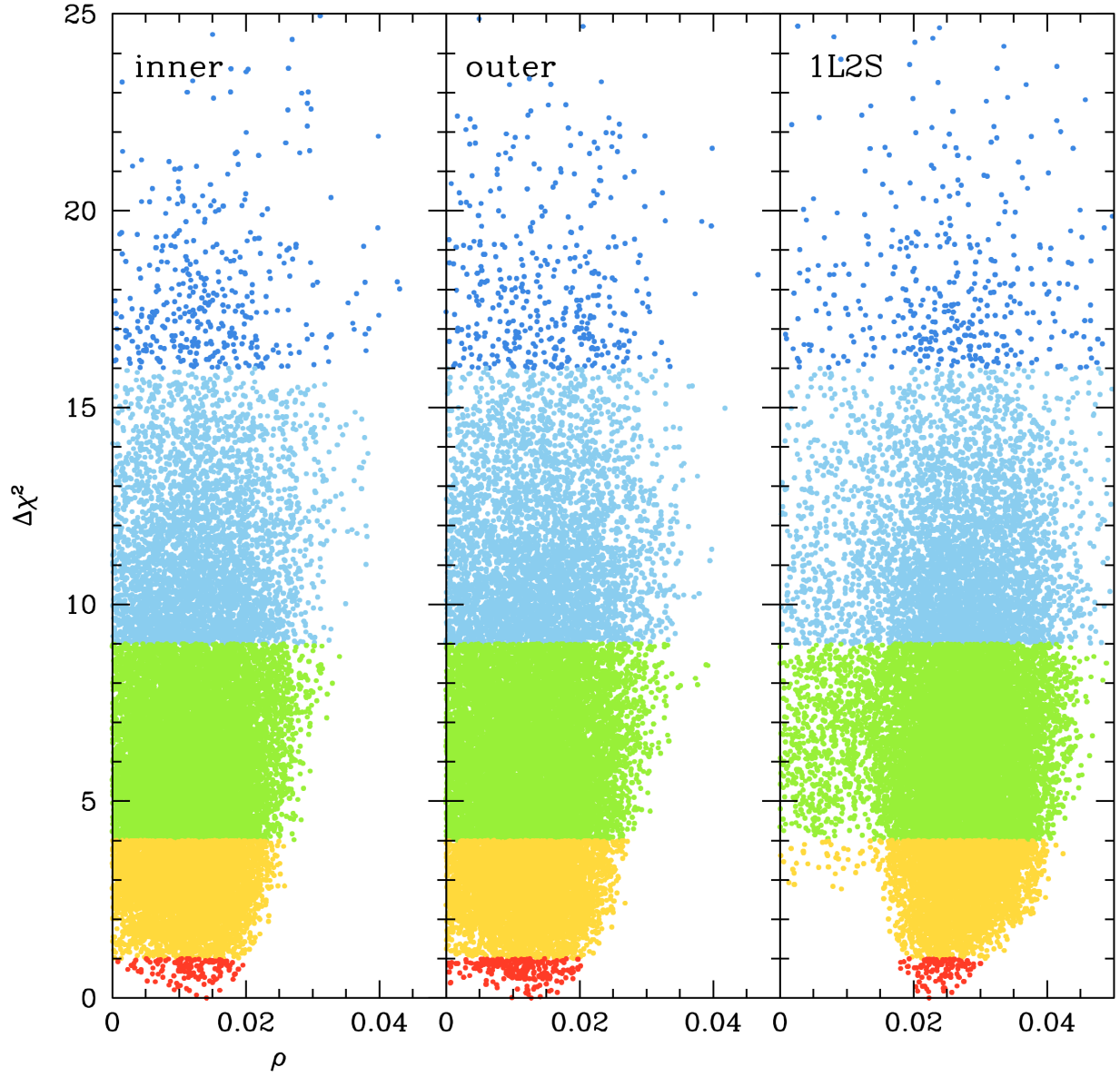


Fig. 19.— Scatter plot of the normalized source radius, ρ , against the values of $\Delta\chi^2$ relative to the best fit for the three solutions of KMT-2023-BLG-0614. Colors indicate values of $\Delta\chi^2 < 1, 4, 9, 16, 25, 36$.

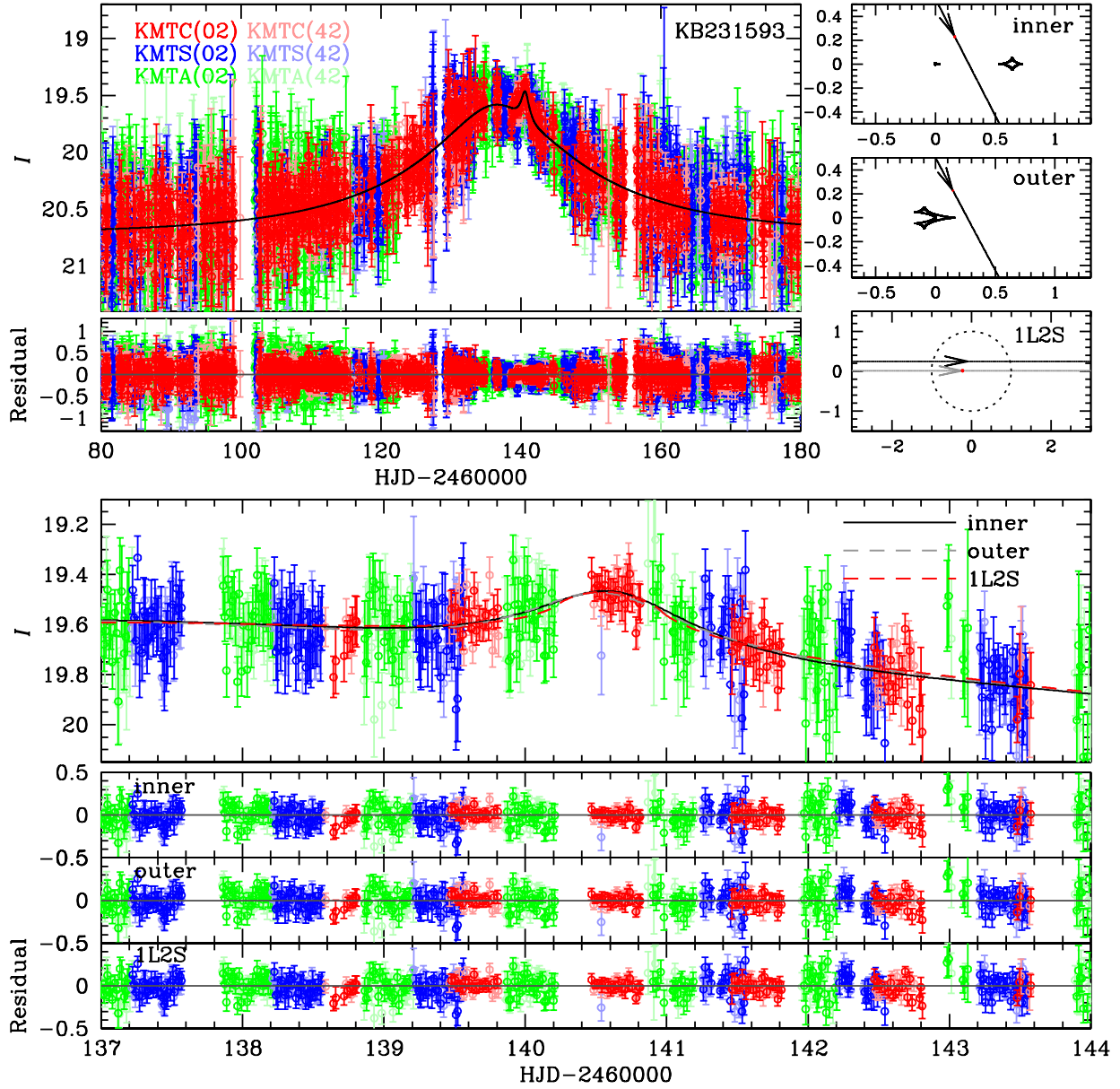


Fig. 20.— Light curve and models for KMT-2023-BLG-1593.

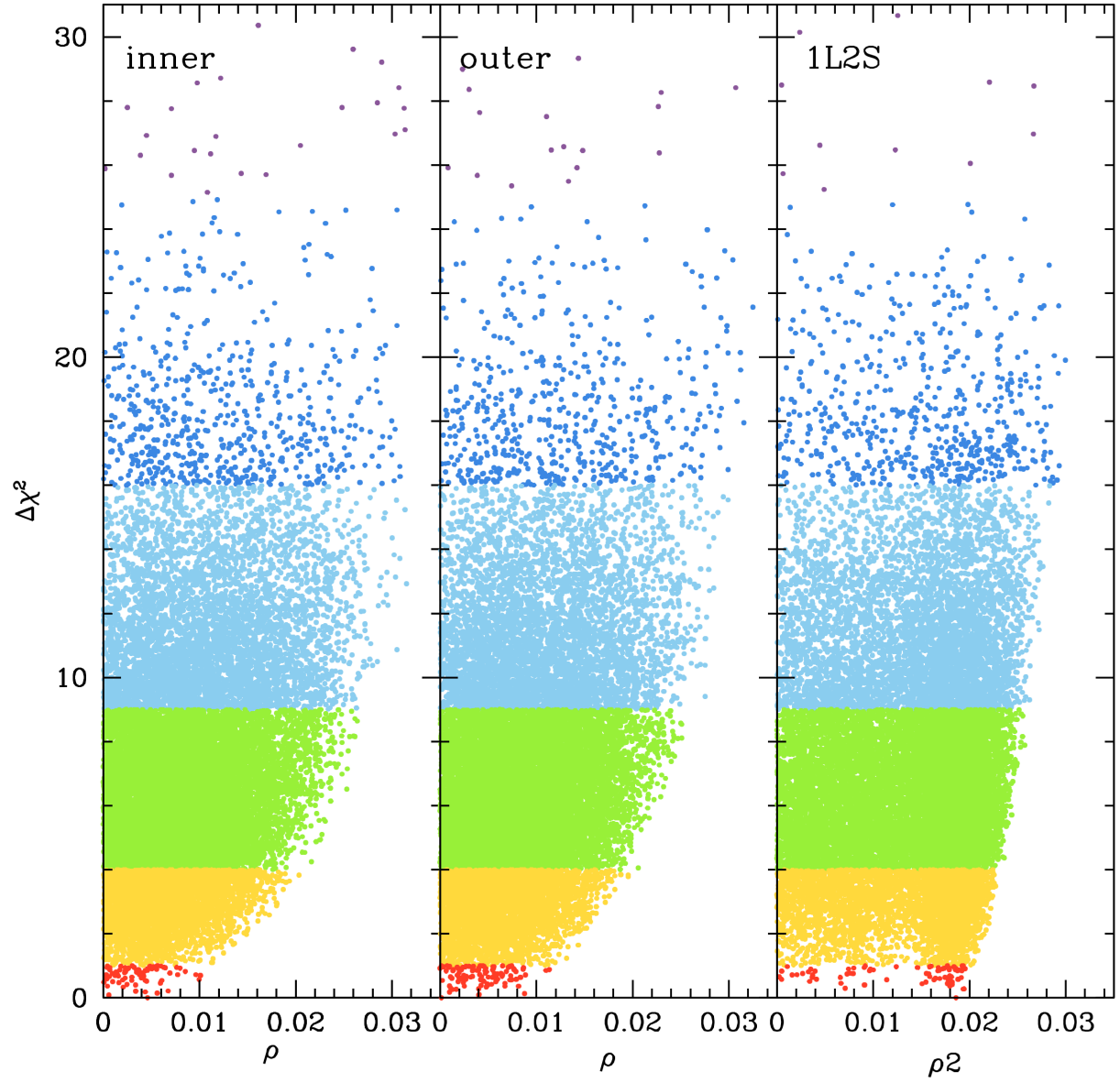


Fig. 21.— Scatter plot of the normalized source radius, ρ , against the values of $\Delta\chi^2$ relative to the best fit for the three solutions of KMT-2023-BLG-1593. Colors indicate values of $\Delta\chi^2 < 1, 4, 9, 16, 25, 36$.